Electronic Supplementary Information for

Highly Efficient TADF-OLEDs with Copper(I) Halide Complexes Containing Unsymmetrically Substituted Thiophenyl Triphosphine

Yu-Ling Liu[a,1], Ruiqin Zhu[b,1], Li Liu[a,*], Xin-Xin Zhong[a,*], Fa-Bao Li[a,*], Guijiang Zhou[b,*], Hai-Mei Qin[c]

[a] *College of Chemistry and Chemical Engineering, Ministry of Education Key Laboratory for the Synthesis and Application of Organic Functional Molecules, Hubei University, Wuhan 430062, P. R. China. E-mail: liulihubei@hubu.edu.cn, xxzhong@hubu.edu.cn, lfb0615@hubu.edu.cn*

[b] *School of Chemistry, Xi'an Jiaotong University, Xi'an 710049, P. R. China. Email: zhougj@mail.xjtu.edu.cn*

[c] *Department of Chemistry, Xiamen University, Xiamen 361005, P. R. China.*

Electronic supplementary information (ESI) available: DETAILS. CCDC 2282047, 2285430, 2297624, 2285431-2285433.

[1] These authors are contributed equally to this work.

Contents

3. Molecular structures

4. Photophysical properties

Figure S35. Normalized excitation spectra of **1–6** in solid state at 297 K.

Figure S36. Temperature dependence of time decay characteristics for complexes **1–6** in the range of 77–297 K in powder state.

5. Computational details

Figure S37. Compositions of the frontier molecular orbitals at optimized S_0 geometry of complex **1**.

Figure S38. Compositions of the frontier molecular orbitals at optimized S_0 geometry of complex **2**.

Figure S39. Compositions of the frontier molecular orbitals at optimized S_0 geometry of complex **3**.

Figure S40. Compositions of the frontier molecular orbitals at optimized S_0 geometry of complex **4.**

Figure S41. Compositions of the frontier molecular orbitals at optimized S_0 geometry of complex **5**.

Figure S42. Compositions of the frontier molecular orbitals at optimized S_0 geometry of complex **6**.

Figure S43. Compositions of the frontier natural transition orbitals at optimized S_1 geometry of complex **1**.

Figure S44. Compositions of the frontier natural transition orbitals at optimized S_1 geometry of complex **2**.

Figure S45. Compositions of the frontier natural transition orbitals at optimized S_1 geometry of complex **3**.

Figure S46. Compositions of the frontier natural transition orbitals at optimized S_1 geometry of complex **4**.

Figure S47. Compositions of the frontier natural transition orbitals at optimized S_1 geometry of complex **5**.

Figure S48. Compositions of the frontier natural transition orbitals at optimized S_1 geometry of complex **6**.

Figure S49. Compositions of the frontier natural transition orbitals at optimized T_1 geometry of complex **1**.

Figure S50. Compositions of the frontier natural transition orbitals at optimized T_1

6. References

1. General information

Materials. All chemicals were purchased from commercial sources and used without being processed unless specified. The starting material in Scheme 1, bis(3-bromothiophen-2-yl)(phenyl)phosphine was synthesized according to the literature method.[1] Tetrahydrofuran (THF) and diethyl ether (Et_2O) were distilled under nitrogen in *the* presence of sodium chips with benzophenone as the indicator before use.

Instrumentation. ^{1}H, ^{13}C and ^{31}P NMR spectra were recorded on a Varian 400 MHz NMR spectrometer using deuterated solvents as the lock and reference. Chemical shifts were referenced to the solvent residual peak at 7.26 ppm for ^{1}H and 77.16 ppm for ^{13}C NMR spectra in $CDCl_3$; at 2.50 ppm for ^{1}H NMR spectra in d_6-DMSO, respectively. High resolution mass spectra (HRMS) were recorded on the Thermo Scientific Exactive Plus equipped with ESI ionization source. The elemental composition was determined with SEM/EDS (Hitachi SU-800 FE-SEM). UV–vis absorption was recorded by a Unicam Helios α spectrometer. Emission spectra and lifetimes of the complexes were measured using Edinburgh instrument FLS980 steady-state and time resolved fluorescence spectrometer (375 nm variable pulsed diode laser, repetition frequencies 1000 Hz, and optical pulse period 100 ns). Solid-state Φ_{PL} values were determined using a Hamamatsu system for absolute PL quantum yield measurements equipped with an integrating sphere with Spectralon inner surface coating. Thermogravimetric analysis (TGA) was performed on a thermal analysis instrument (Perkin-Elmer Diamond) under nitrogen atmosphere at a heating rate of 20 °C min^{-1}. Differential scanning calorimetry (DSC) was performed on a thermal analysis instrument (NETZSCH 214 polyma) under nitrogen atmosphere at a

heating rate of 10 °C min^{-1}. The cyclic voltammetric measurements were carried out with CHI660E.

X-ray crystallography. Crystals of complexes **1–6** suitable for X-ray diffraction studies were grown by slow evaporation of their respective solutions in CH_2Cl_2/MeCN or CH_2Cl_2/*n*-hexane or CH_2Cl_2/ethanol at room temperature. Geometric and intensity data were collected using Cu Kα radiation (λ = 1.54184 Å) on a XtaLAB Synergy, Dualflex, HyPix area detector. The collected frames were processed with the software *SAINT*[2], and an absorption correction was applied (*SADABS*)[3] to the collected reflections. The structures were solved by direct methods (*SHELXTL*)[4] in conjunction with standard difference Fourier techniques and subsequently refined by full-matrix least-squares analyses on F^2. All non-hydrogen atoms were assigned with anisotropic displacement parameters.

Theoretical calculations. The structural parameters for complexes **1–6** were obtained from the crystal data which are listed in Tables 1 and 2. The corresponding ground-state (S_0) geometries were all optimized at theoretical level of B3LYP-D3(BJ)/6-311+G(d,p) (LANL2D2 for Cu and I atoms), where D3(BJ) was Grimme's D3 dispersion correction with Becke-Jonson damping. To calculate the adiabatic excitation energies, the optimized geometries of S_1 and T_1 are required, which were obtained at theoretical levels of TD-B3LYP-D3(BJ)/6-31+G(d) and UB3LYP-D3(BJ)/6-31+G(d) (LANL2D2 for Cu and I atoms), respectively. The absorption spectra based on the optimized S_0 geometries were obtained at the TD-B3LYP-D3(BJ)/6-311+G(d,p) (LANL2D2 for Cu and I atoms) level. In addition, the solvent effects were taken into account by the polarizable continuum model (PCM, solvent = dichloromethane) for the purpose of comparing with the experimental spectra. All the calculations were manipulated by the Gaussian 16 suite.[5] The compositions of the frontier molecular and natural transition orbitals at optimized S_0, S_1 and T_1 geometries

of complex **1–6** were calculated by the Multiwfn program.[6,7]

Cyclic voltammetric measurement. Experiments were performed at room temperature in a homemade airtight three–electrode cell connected to a nitrogen gas injection. The reference electrode consisted of a saturated calomel electrode (SCE). The counter electrode was a platinum wire counter electrode. The working electrode was a glassy carbon electrode (3 mm diameter). The supporting electrolyte tetrabutylammonium hexafluorophosphate (n-Bu_4N)(PF_6) (Macklin, 98%) was used as received and simply degassed under nitrogen. Dichloromethane was freshly distilled over CaH_2 prior to use. The solutions used during the electrochemical studies were typically 2×10^{-3} M in complex compound and 0.1 M in supporting electrolyte. Before each measurement, the solutions were degassed by bubbling N_2 and the working electrode was polished with 0.05 micron gamma Alumina power on suede, and then the working electrodes were ultrasonically treated with acetone.

Device fabrication. Electroluminescent (EL) devices were fabricated by the conventional vacuum deposition method under a pressure of less than 5×10^{-4} Pa. The devices were made on an indium-tin oxide (ITO) film (15 Ω per square, thickness 110 nm) with a 9 mm^2 square-patterned area. The EL spectra, CIE coordinates and J–V–L curves of the devices were measured with a PHOTO RESEARCH SpectraScan PR 655 photometer and a KEITHLEY 2400 SourceMeter constant current source. The EQE values were calculated by assuming a lambertian emission pattern.

2. NMR and mass spectra

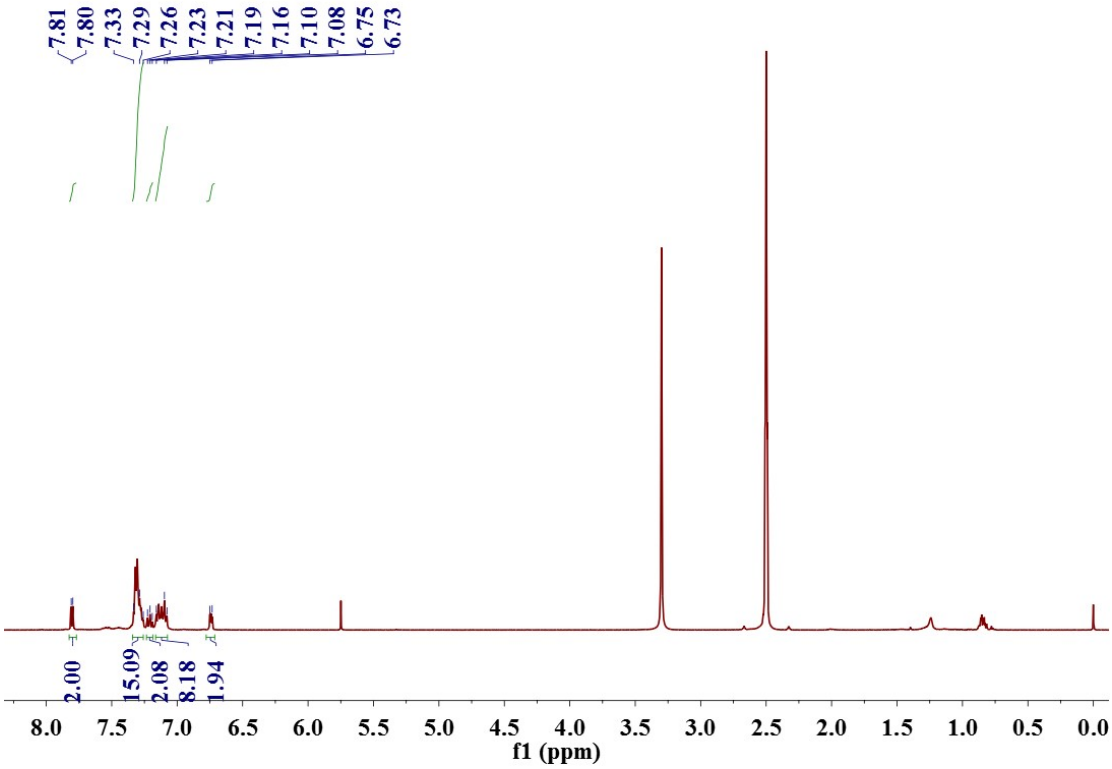

Figure S1. ^{1}H NMR spectrum of **L1** in d_6-DMSO.

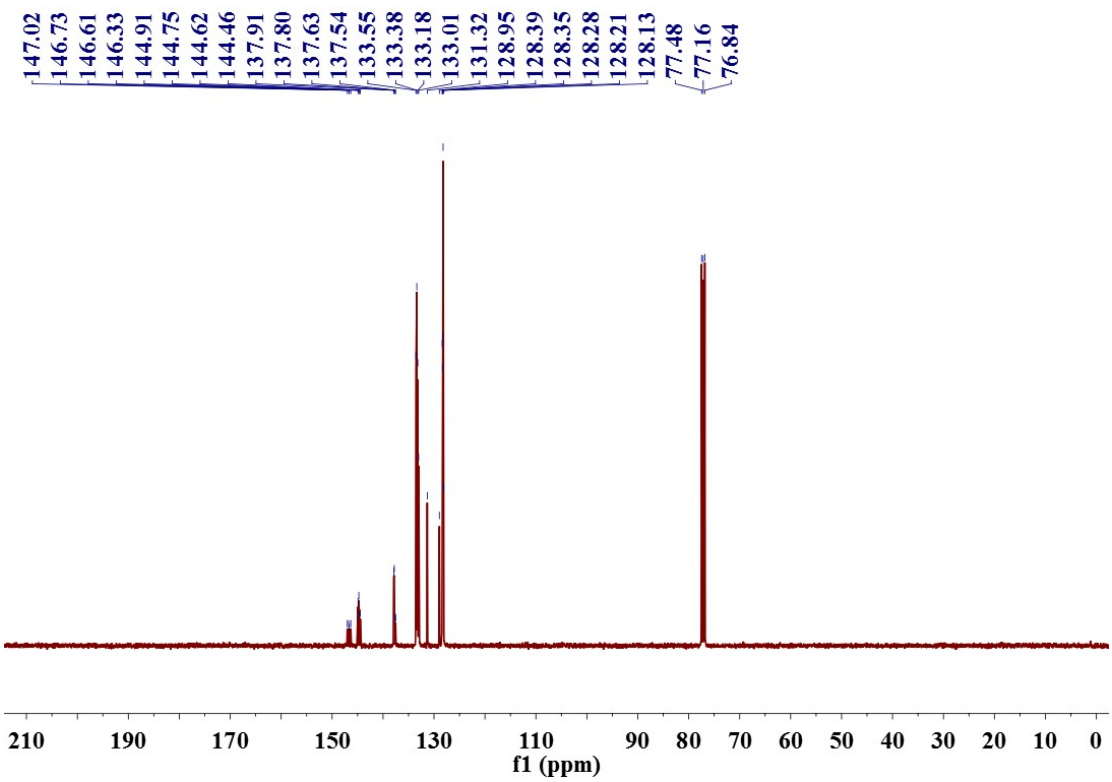

Figure S2. ^{13}C NMR spectrum of **L1** in $CDCl_3$.

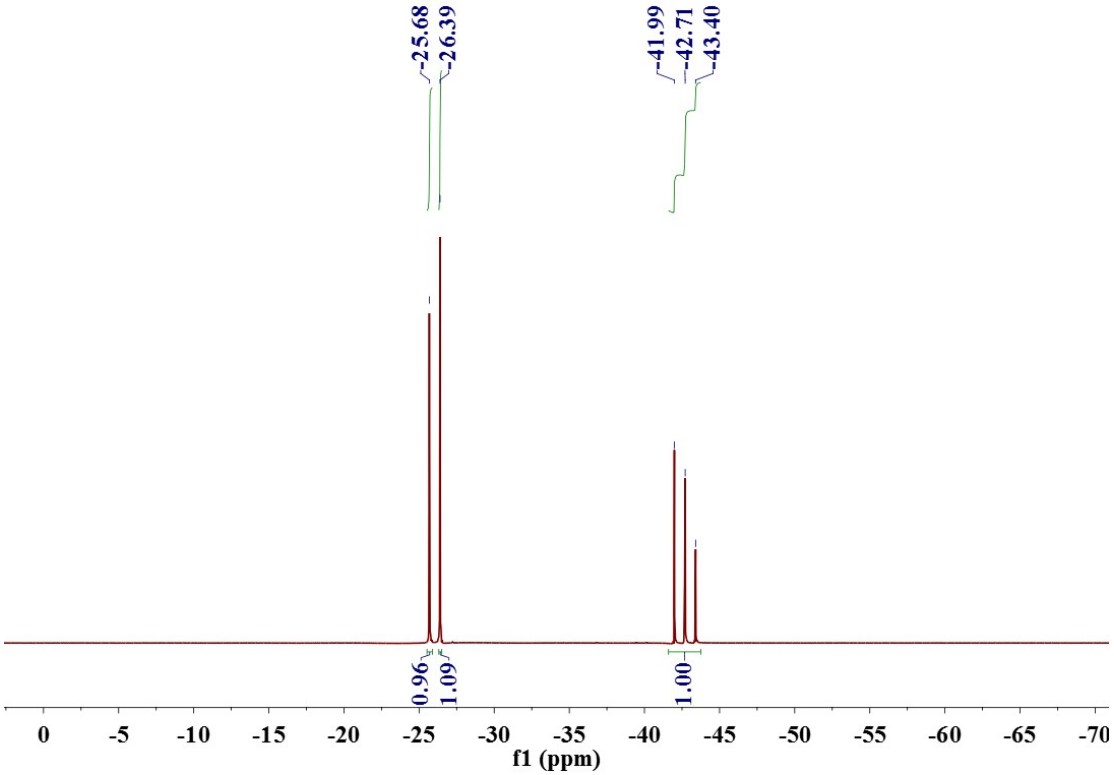

Figure S3. ^{31}P NMR spectrum of **L1** in $CDCl_3$.

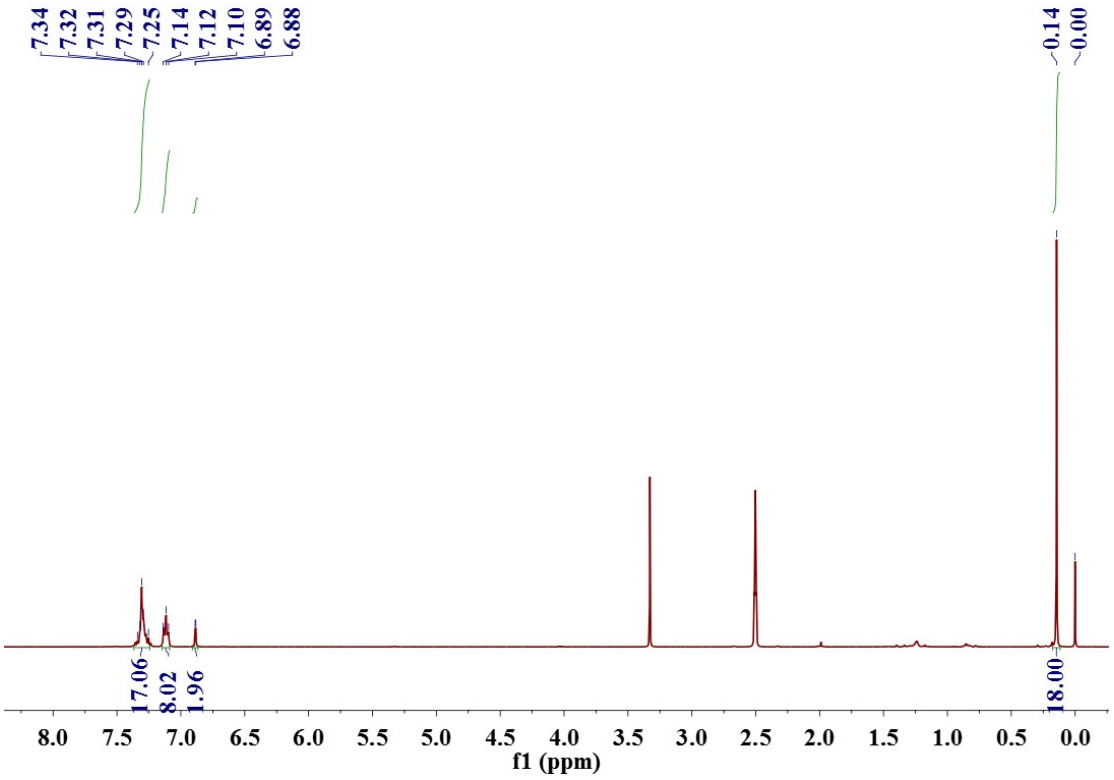

Figure S4. ^{1}H NMR spectrum of **L2** in d_6-DMSO.

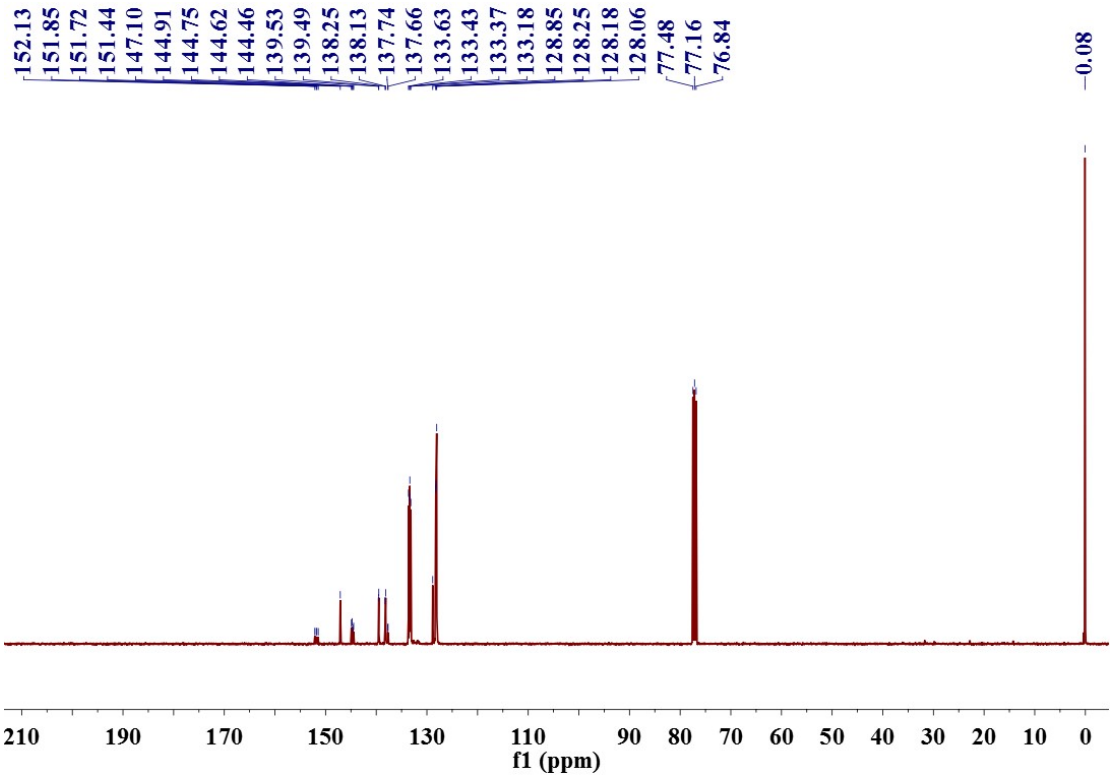

Figure S5. ^{13}C NMR spectrum of **L2** in $CDCl_3$.

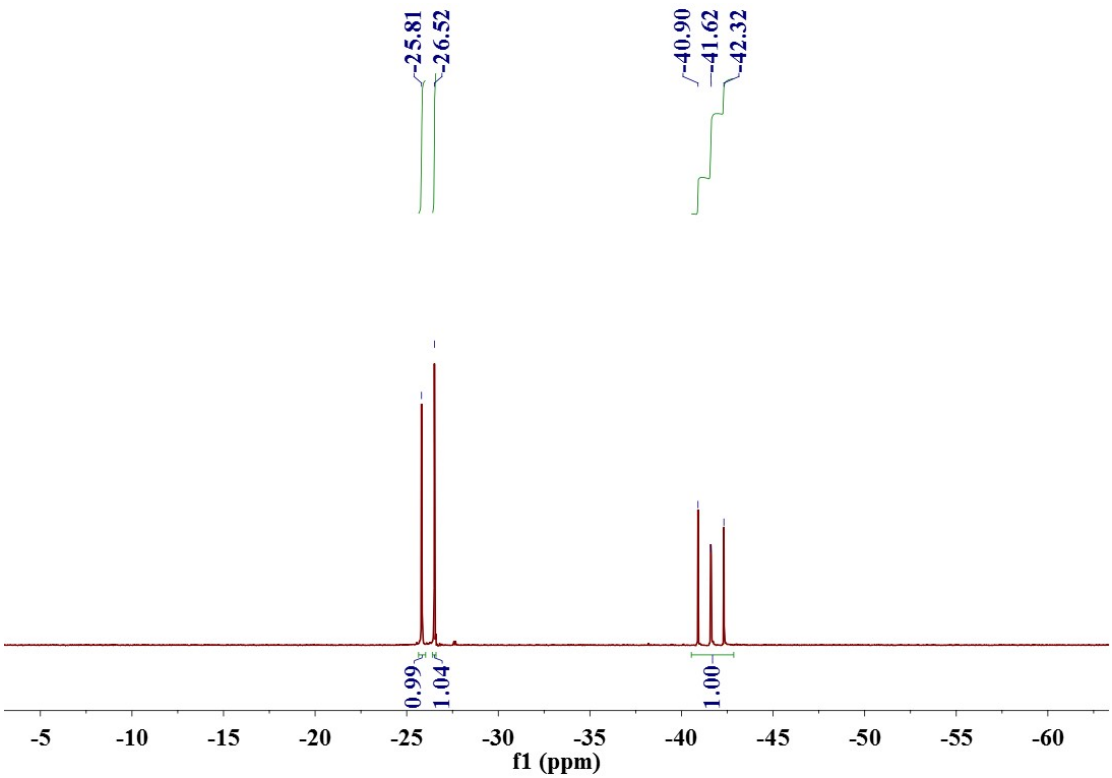

Figure S6. ^{31}P NMR spectrum of **L2** in $CDCl_3$.

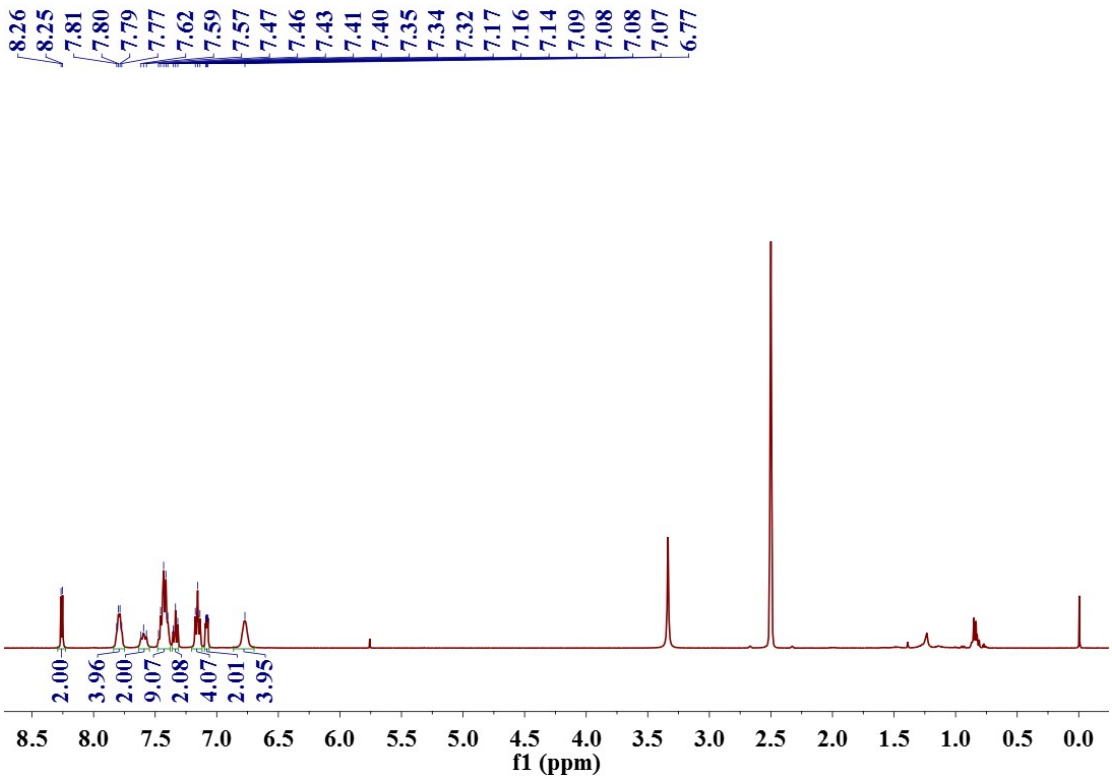

Figure S7. ^{1}H NMR spectrum of **1** in d_6-DMSO.

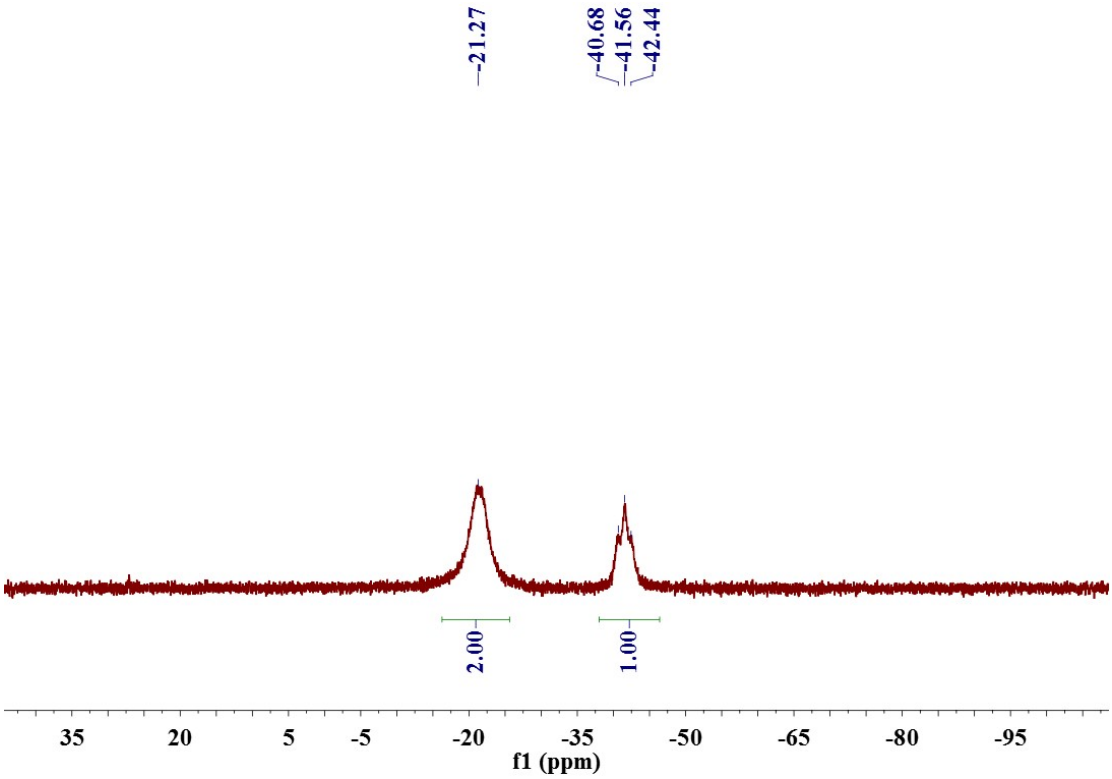

Figure S8. ^{31}P NMR spectrum of **1** in $CDCl_3$.

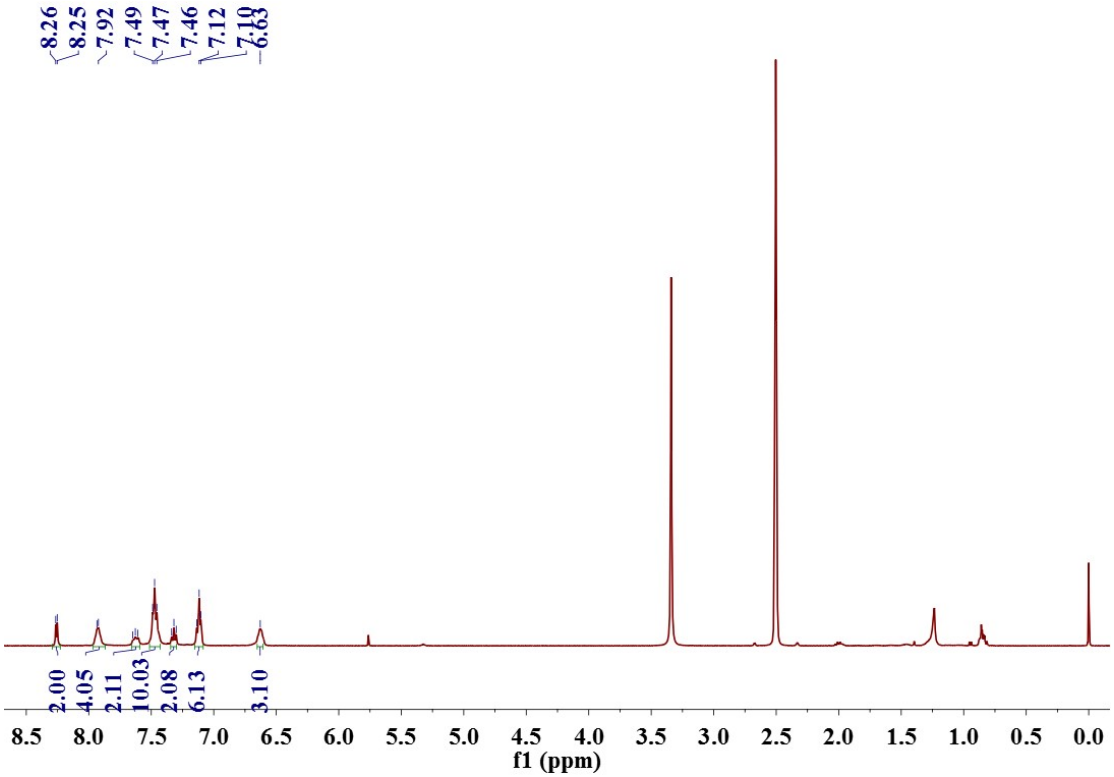

Figure S9. ^{1}H NMR spectrum of **2** in d_6-DMSO.

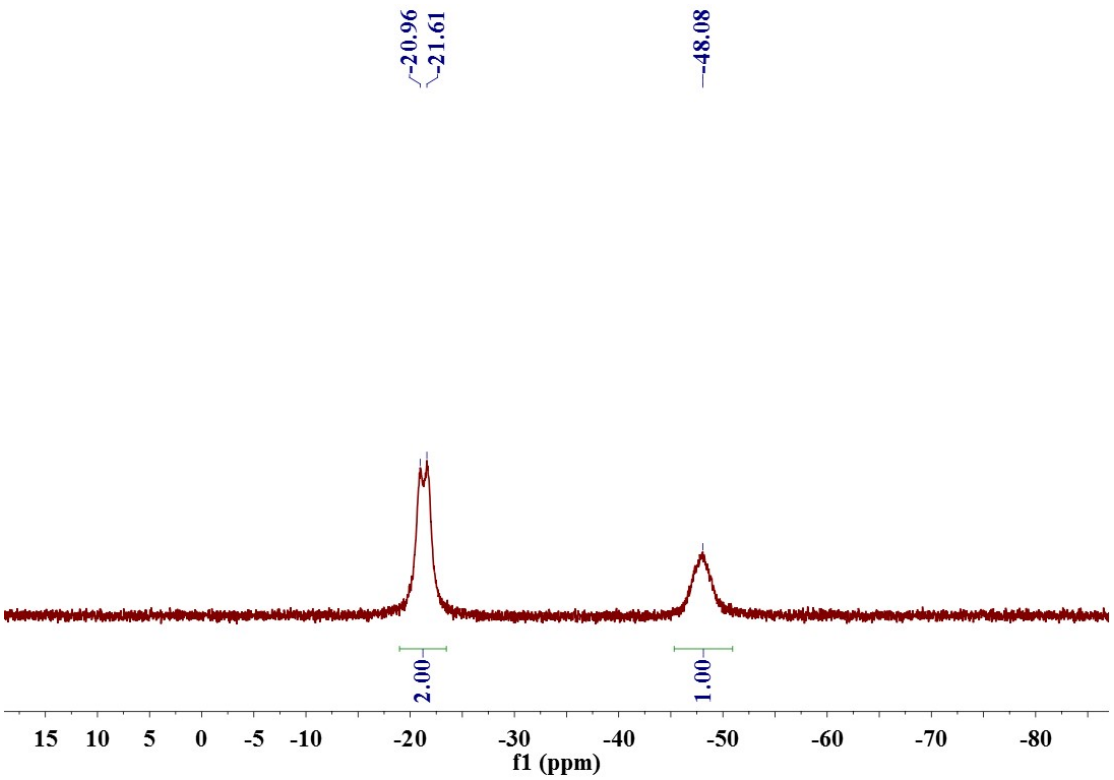

Figure S10. ^{31}P NMR spectrum of **2** in $CDCl_3$.

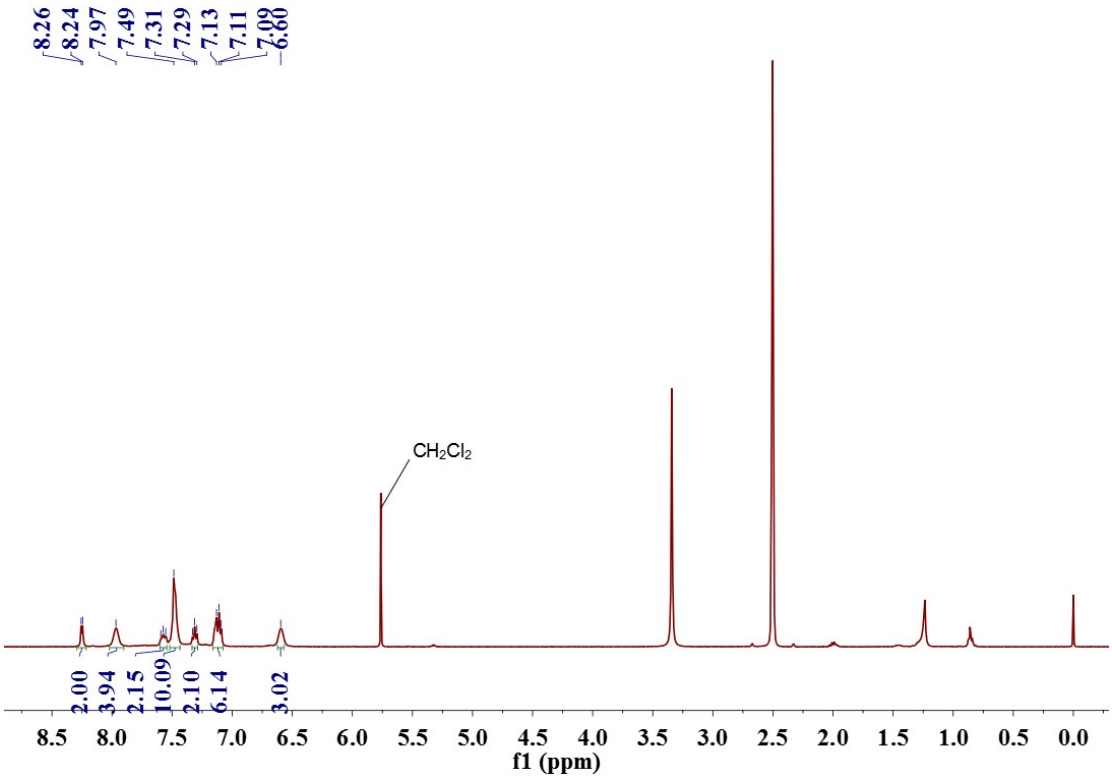

Figure S11. ^{1}H NMR spectrum of **3** in d_6-DMSO.

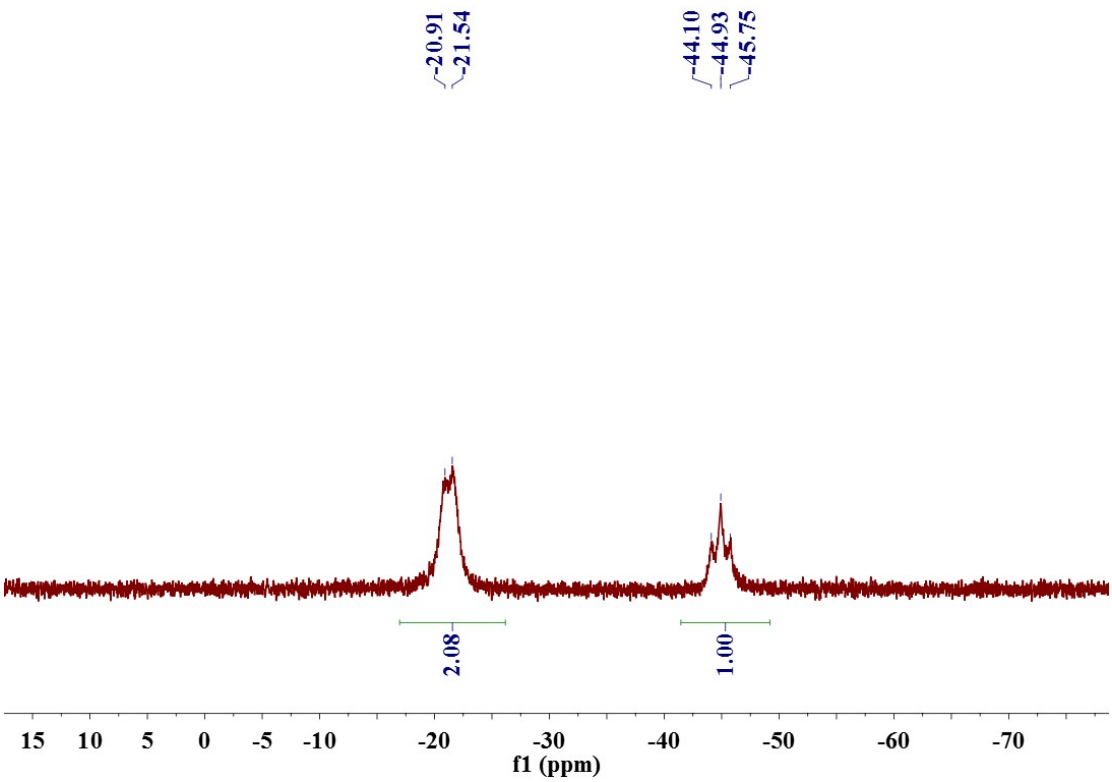

Figure S12. ^{31}P NMR spectrum of **3** in $CDCl_3$.

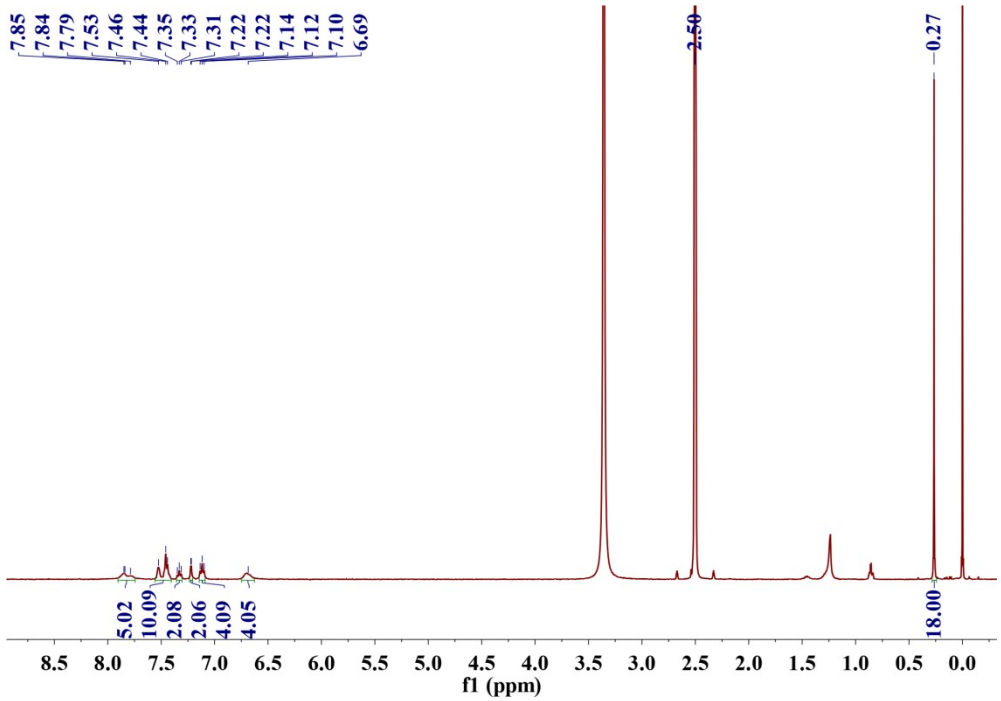

Figure S13. ^{1}H NMR spectrum of **4** in d_6-DMSO.

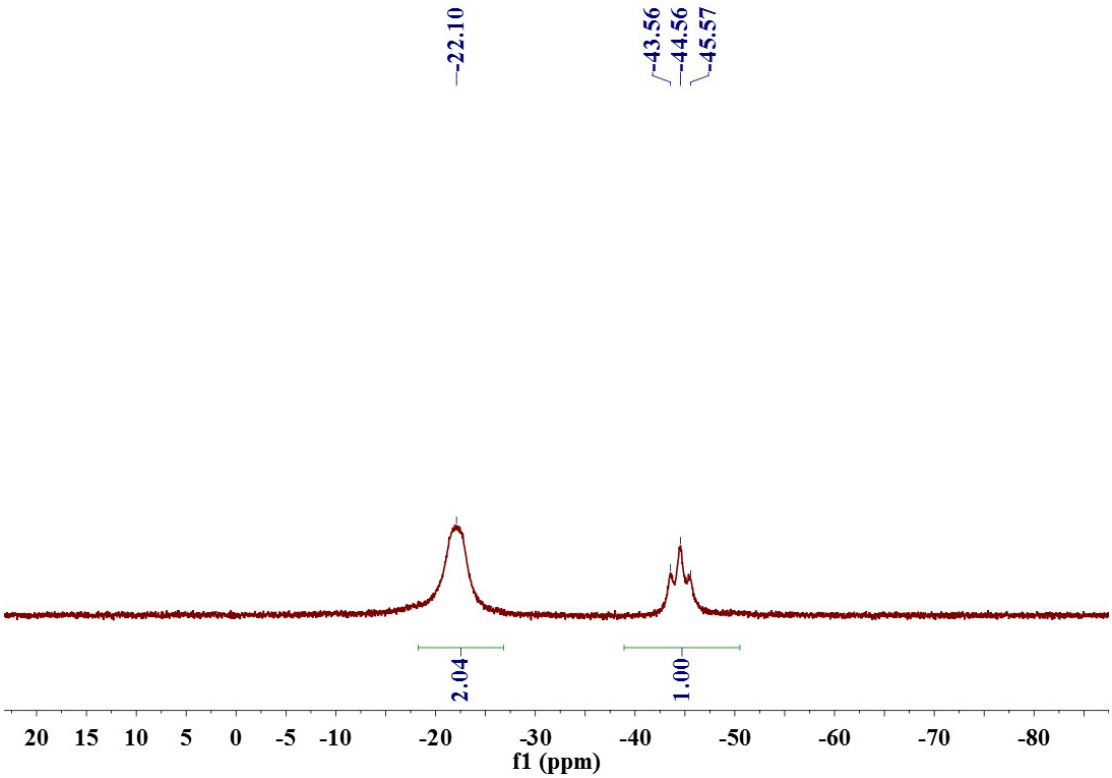

Figure S14. ^{31}P NMR spectrum of **4** in $CDCl_3$.

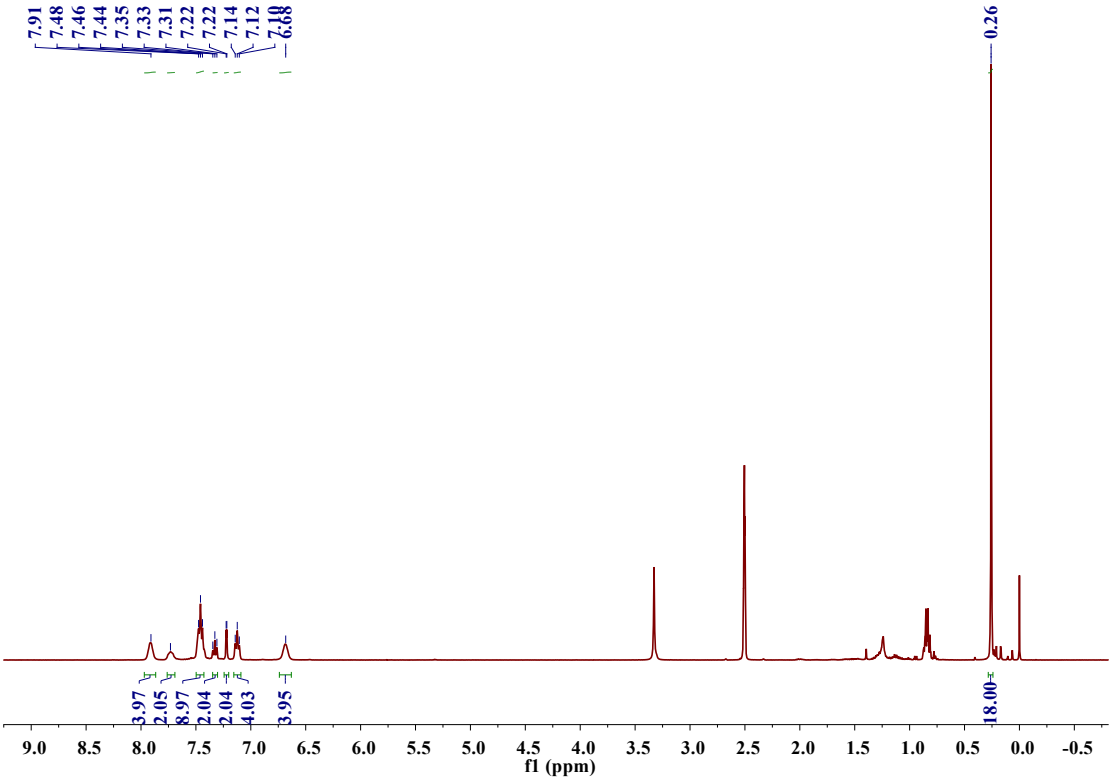

Figure S15. ^{1}H NMR spectrum of **5** in d_6-DMSO.

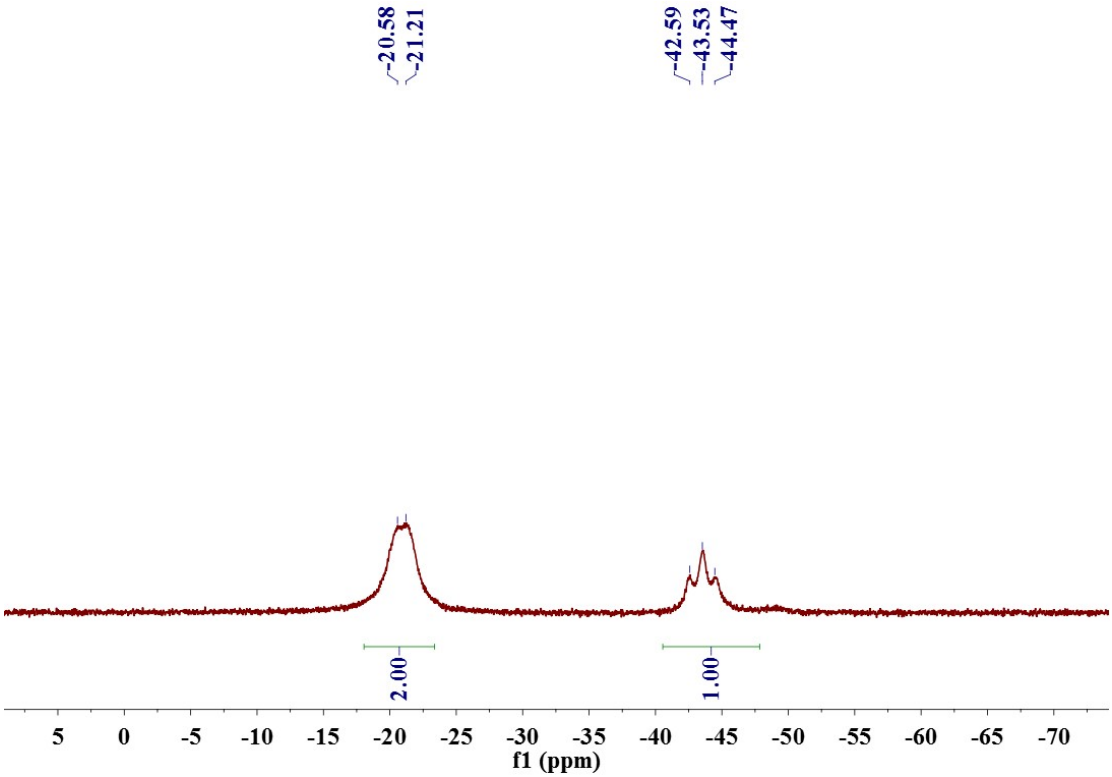

Figure S16. ^{31}P NMR spectrum of **5** in $CDCl_3$.

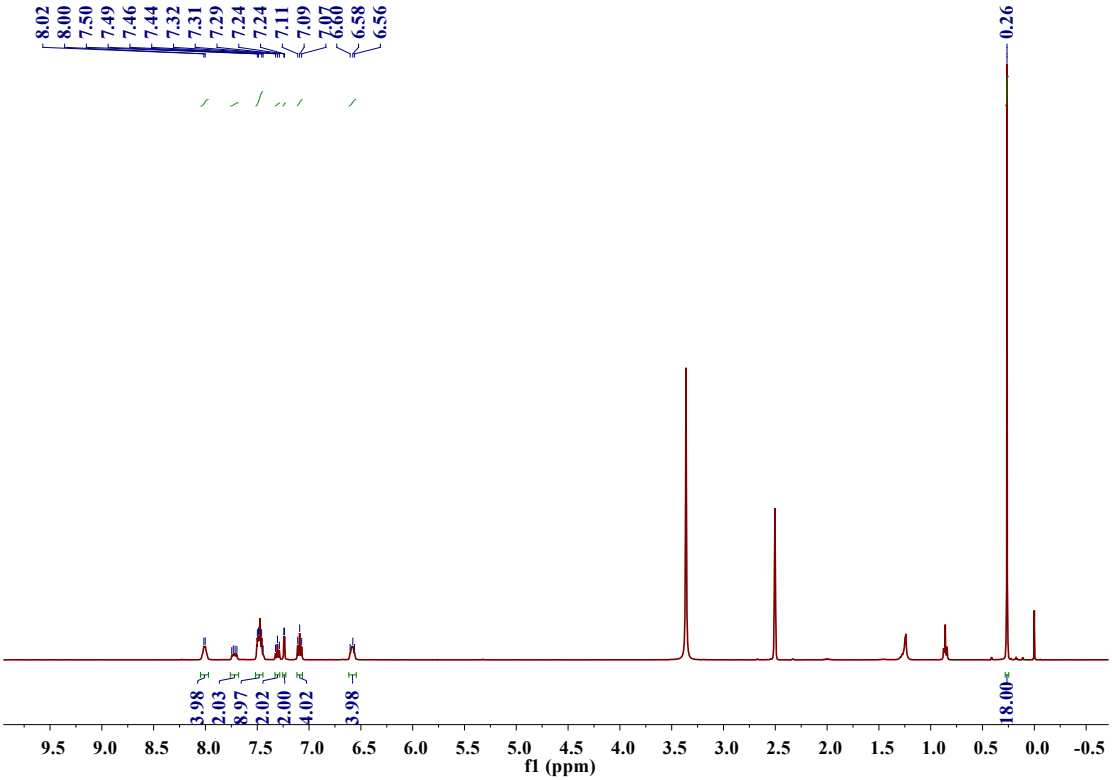

Figure S17. ^{1}H NMR spectrum of **6** in d_6-DMSO.

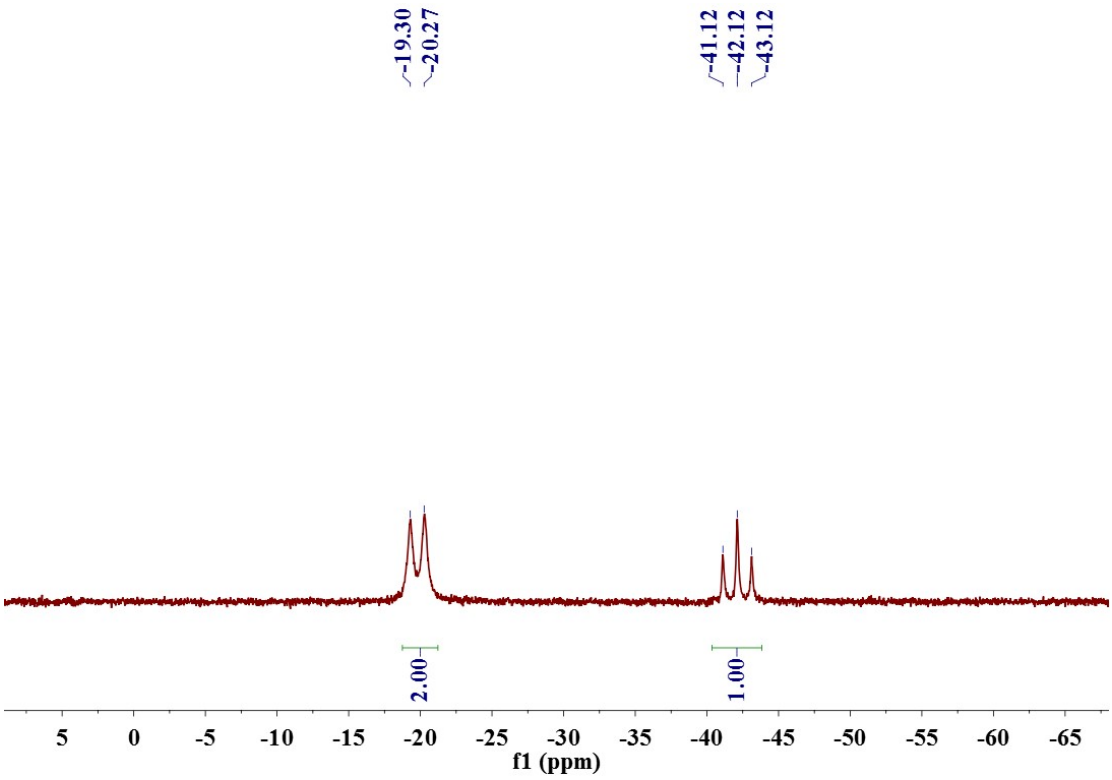

Figure S18. ^{31}P NMR spectrum of **6** in d_6-DMSO.

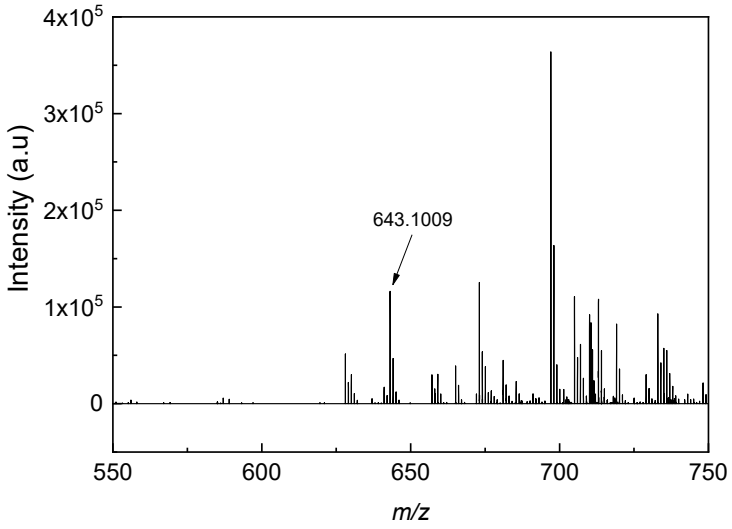

Figure S19. Mass spectrum of **L1**.

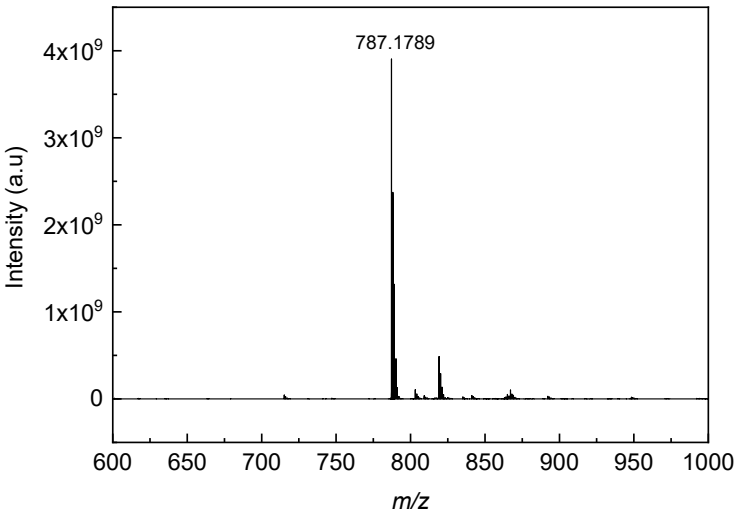

Figure S20. Mass spectrum of **L2**.

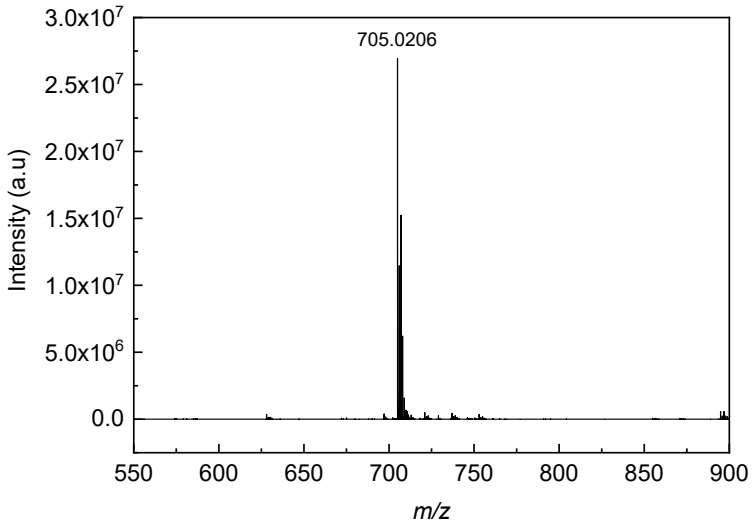

Figure S21. Mass spectrum of **1**.

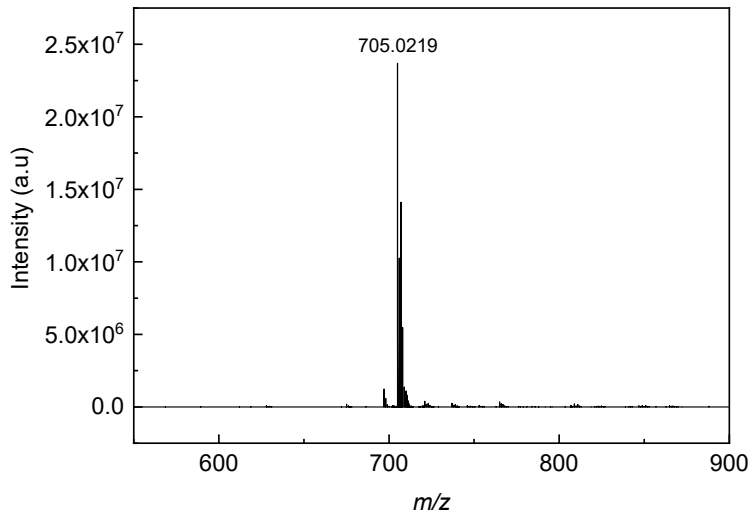

Figure S22. Mass spectrum of **2**.

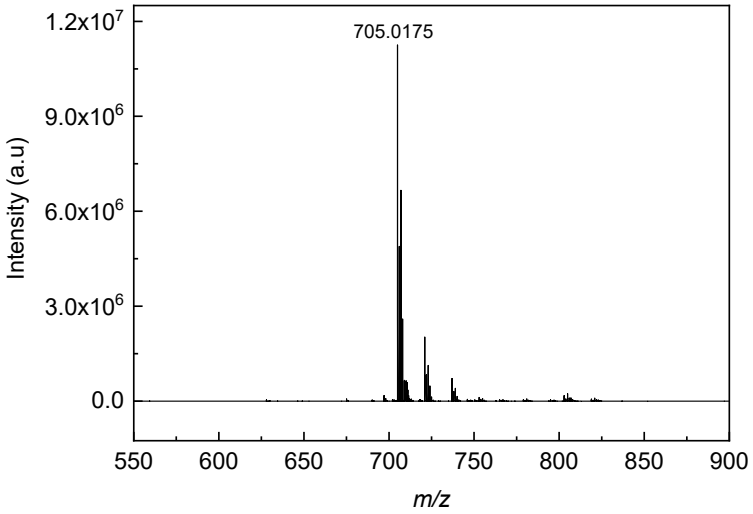

Figure S23. Mass spectrum of **3**.

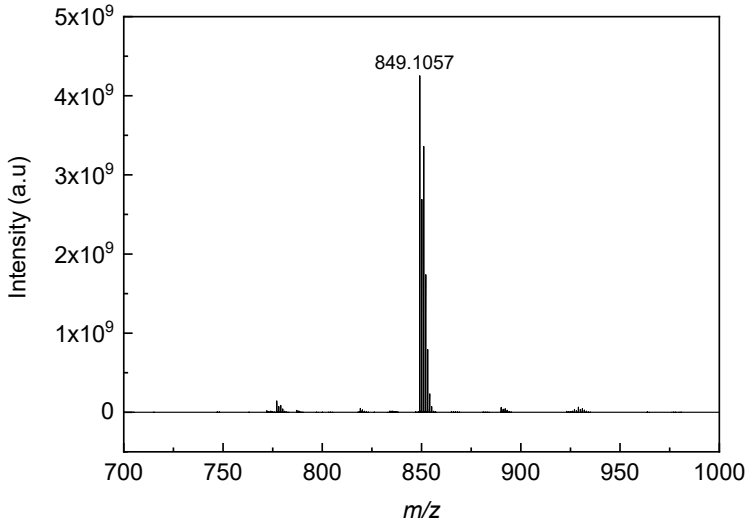

Figure S24. Mass spectrum of **4**.

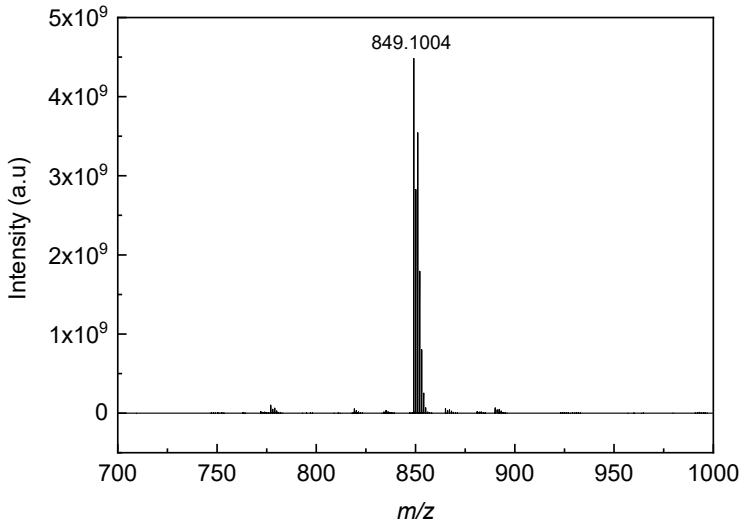

Figure S25. Mass spectrum of **5**.

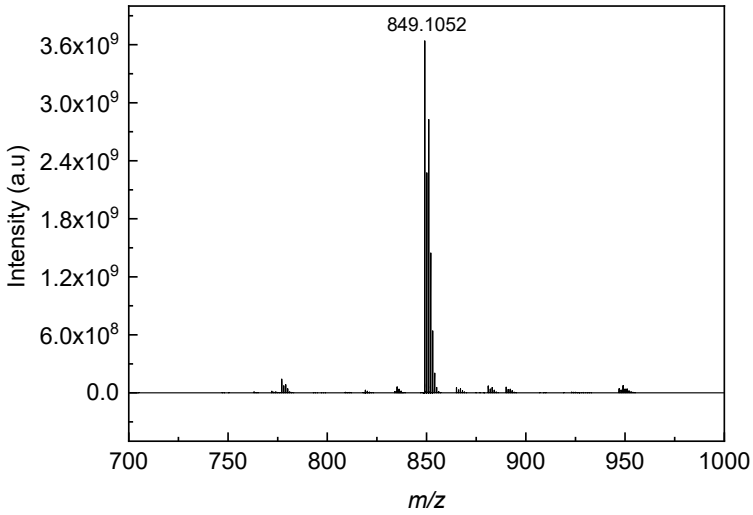

Figure S26. Mass spectrum of **6**.

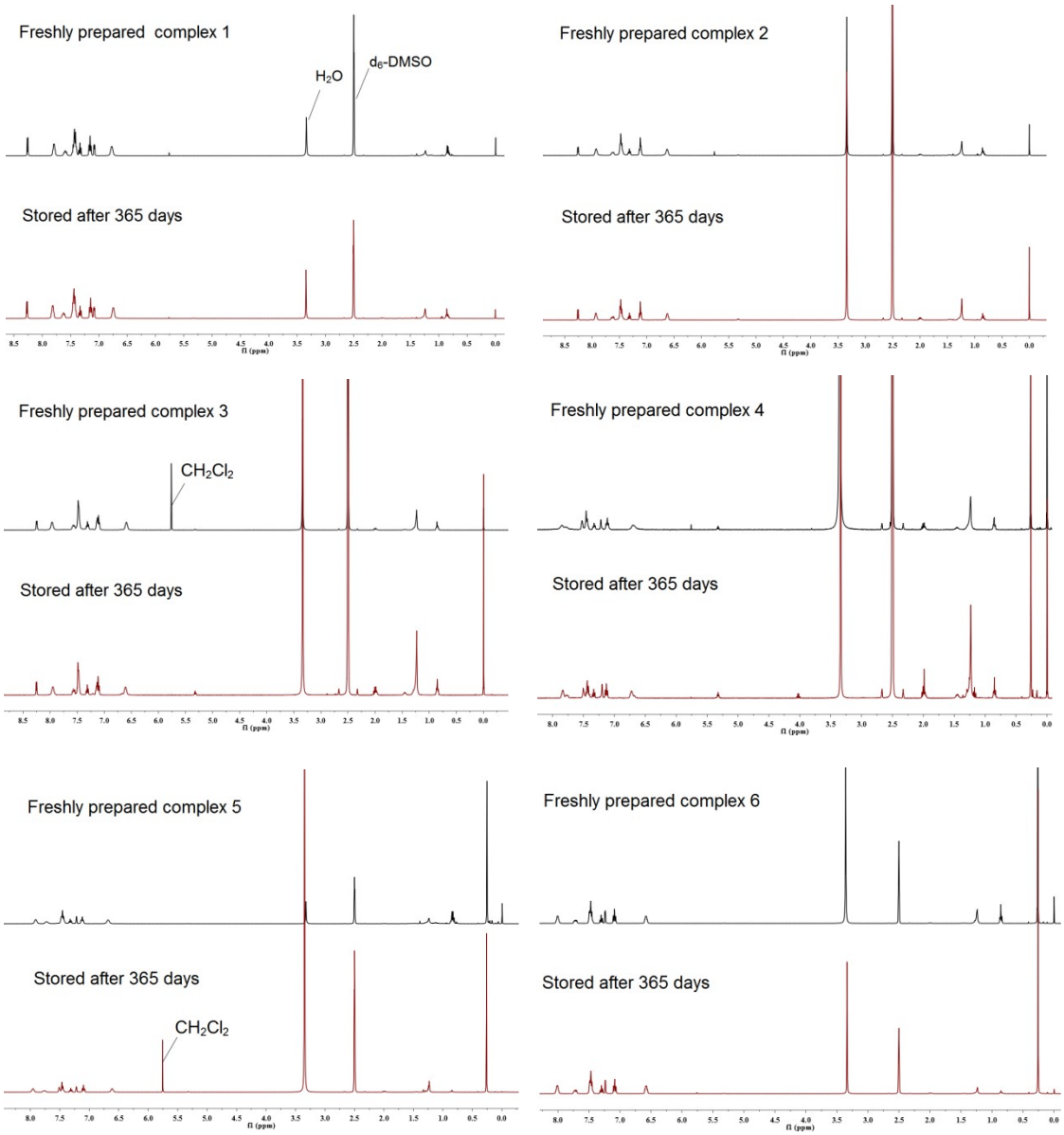

Figure S27. ^{1}H NMR spectra of complexes **1–6** from the freshly prepared sample and the sample stored after 365 days.

3. Molecular structures

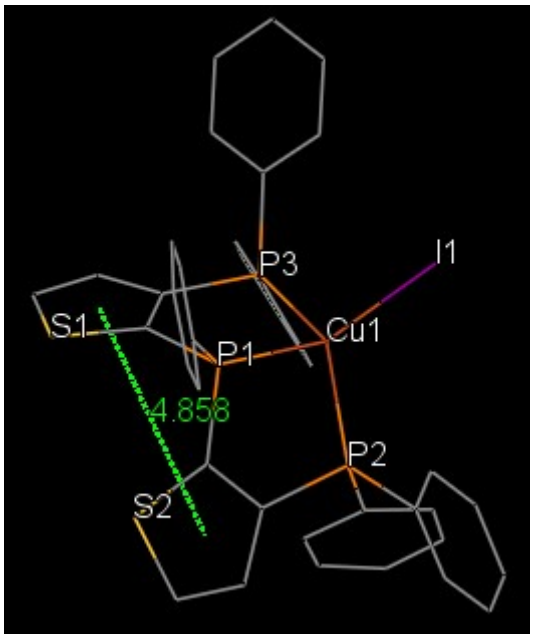

Figure S28. The distance between the two centroids of the two thiophenyl rings in **1**.

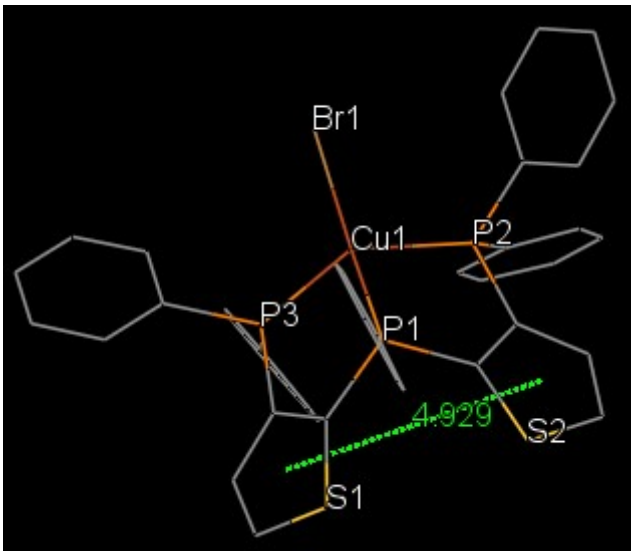

Figure S29. The distance between the two centroids of the two thiophenyl rings in **2**.

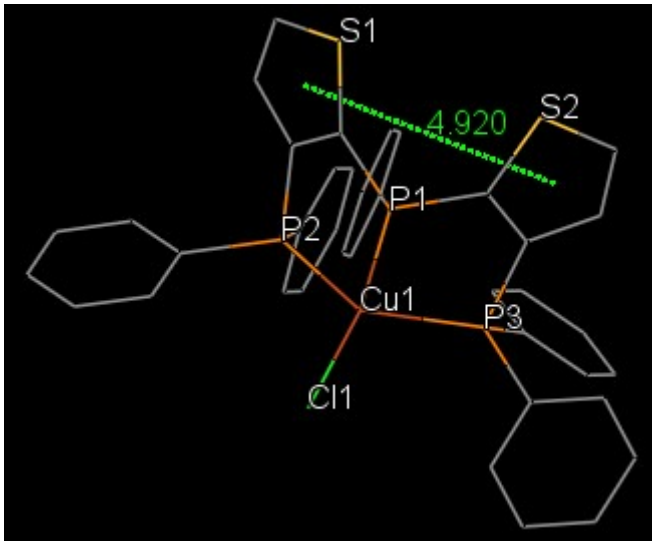

Figure S30. The distance between the two centroids of the two thiophenyl rings in **3**.

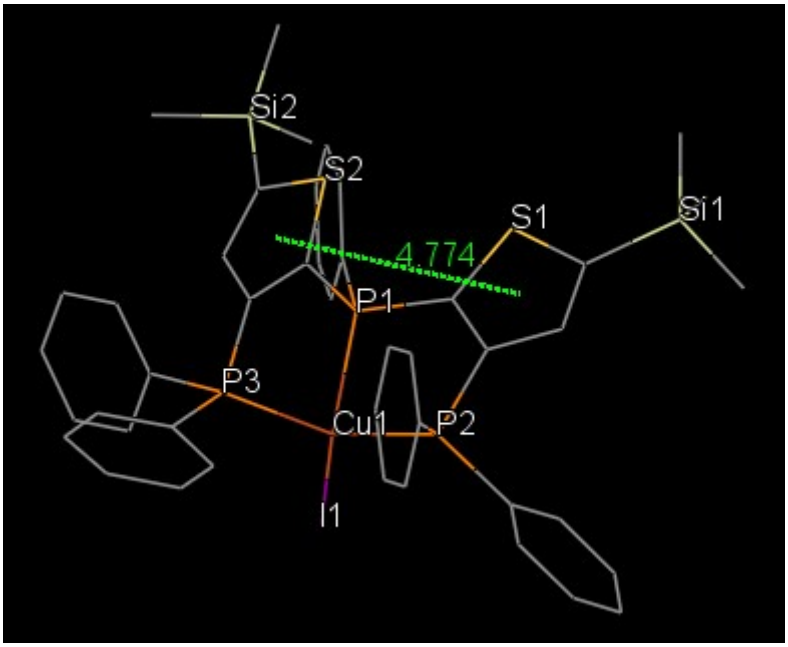

Figure S31. The distance between the two centroids of the two thiophenyl rings in **4**.

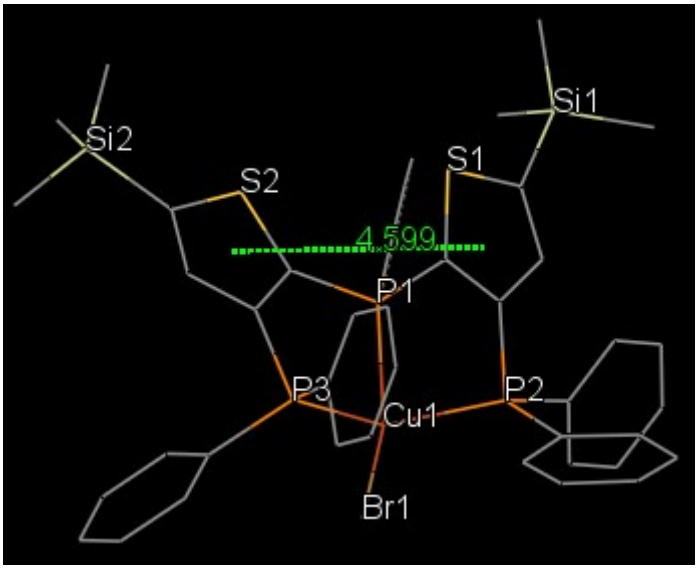

Figure S32. The distance between the two centroids of the two thiophenyl rings in **5**.

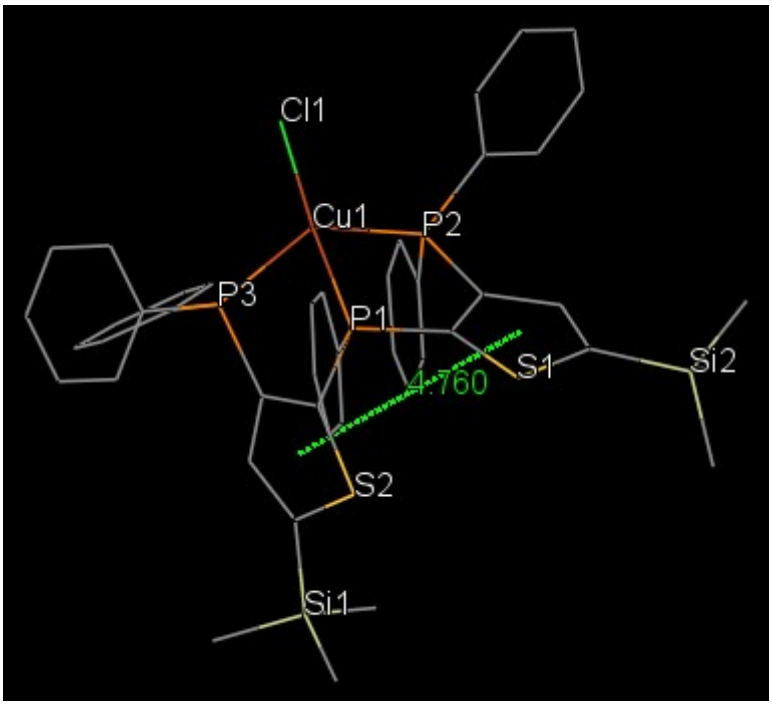

Figure S33. The distance between the two centroids of the two thiophenyl rings in **6**.

4. Photophysical properties

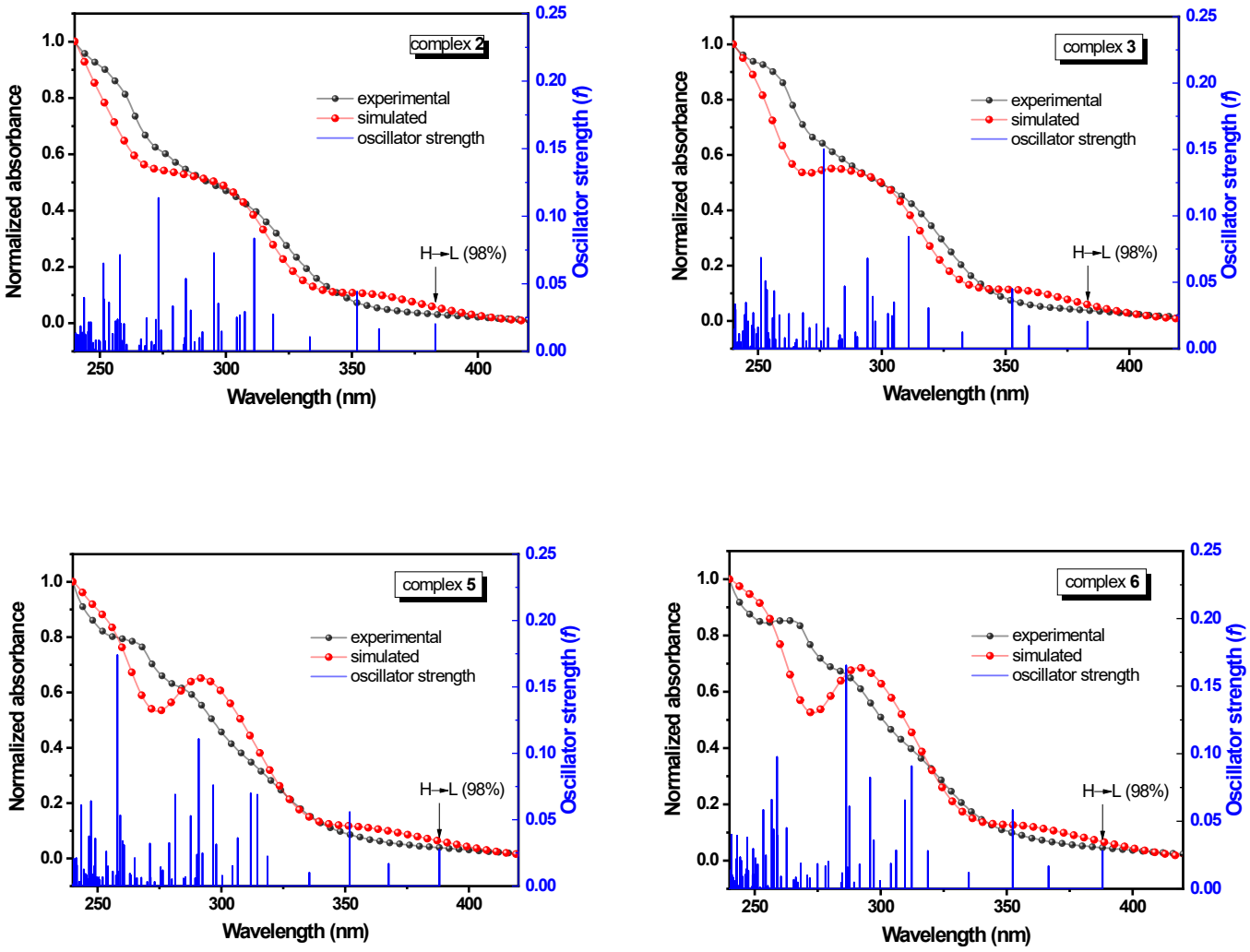

Figure S34. Experimental UV-vis absorption spectra and simulated spectra with oscillator strength for complexes **2**, **3**, **5** and **6**.

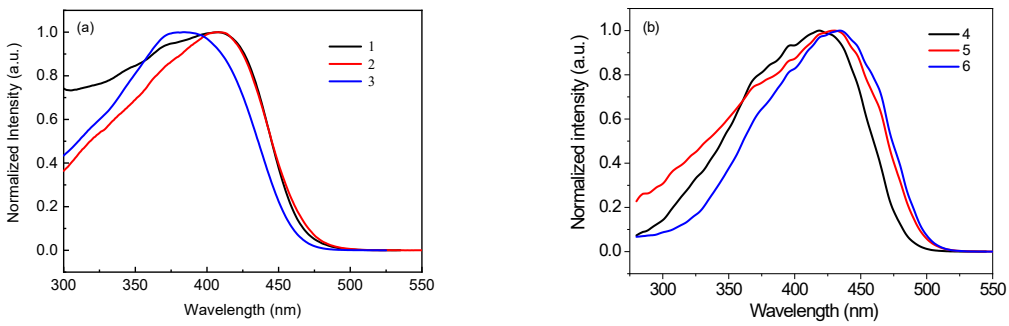

Figure S35. Normalized excitation spectra of **1–6** in powder state at 297 K (λ_{em}, **1**: 554 nm; **2**: 585 nm; **3**: 580 nm; **4**: 565 nm; **5**: 580 nm; **6**: 590 nm).

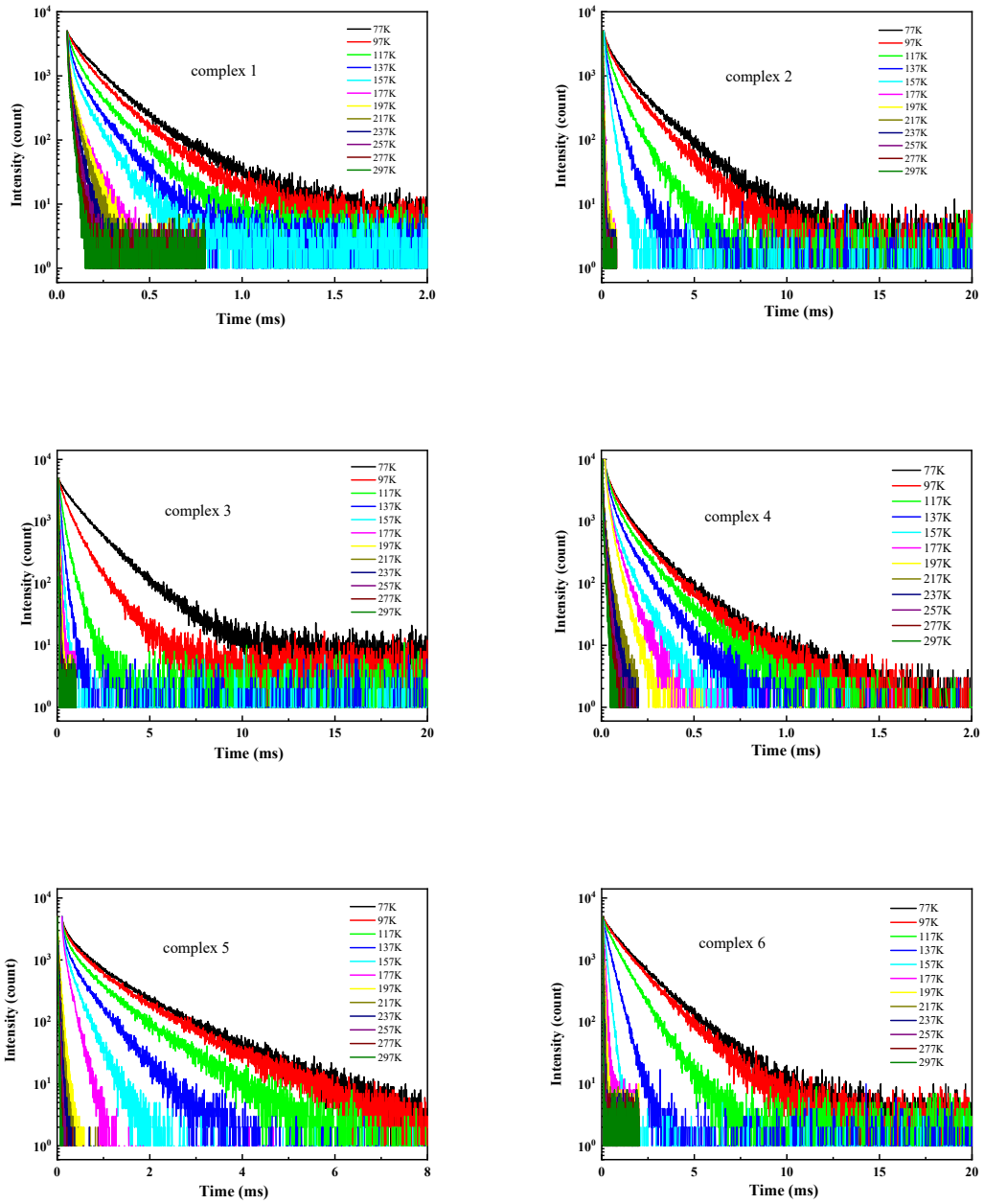

Figure S36. Temperature dependence of time decay characteristics for complexes **1–6** in the range of 77–297 K in powder state.

5. Computational details

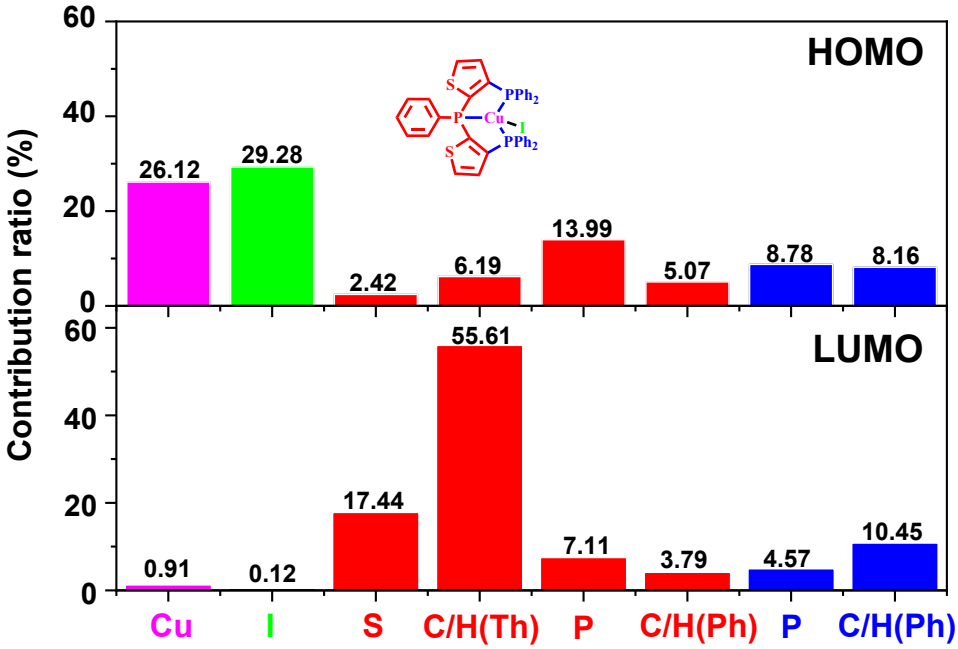

Figure S37. Compositions of the frontier molecular orbitals at optimized S_0 geometry of complex **1**.

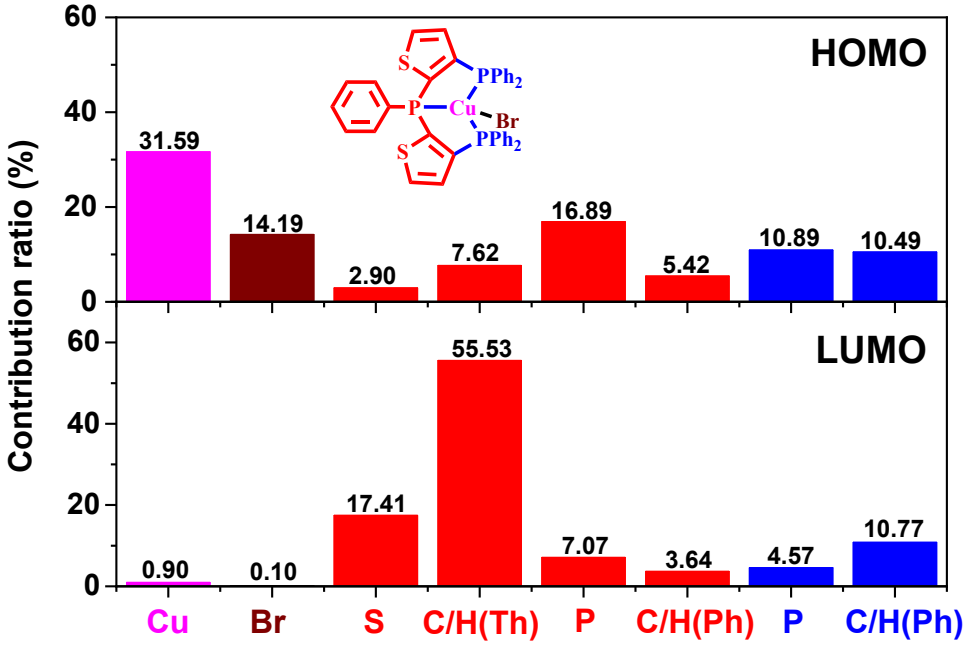

Figure S38. Compositions of the frontier molecular orbitals at optimized S_0 geometry of complex **2**.

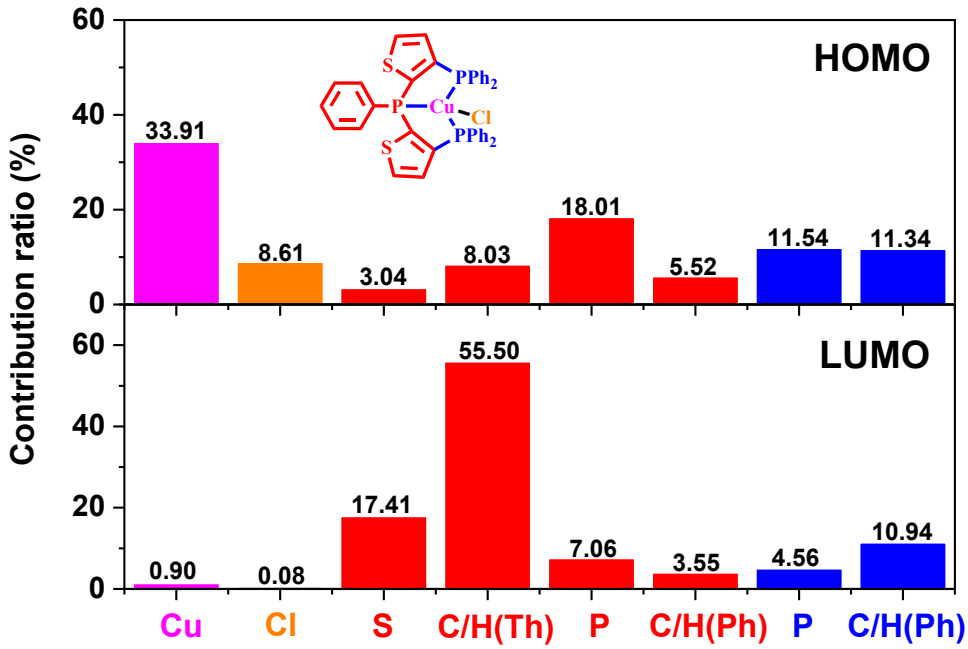

Figure S39. Compositions of the frontier molecular orbitals at optimized S_0 geometry of complex **3**.

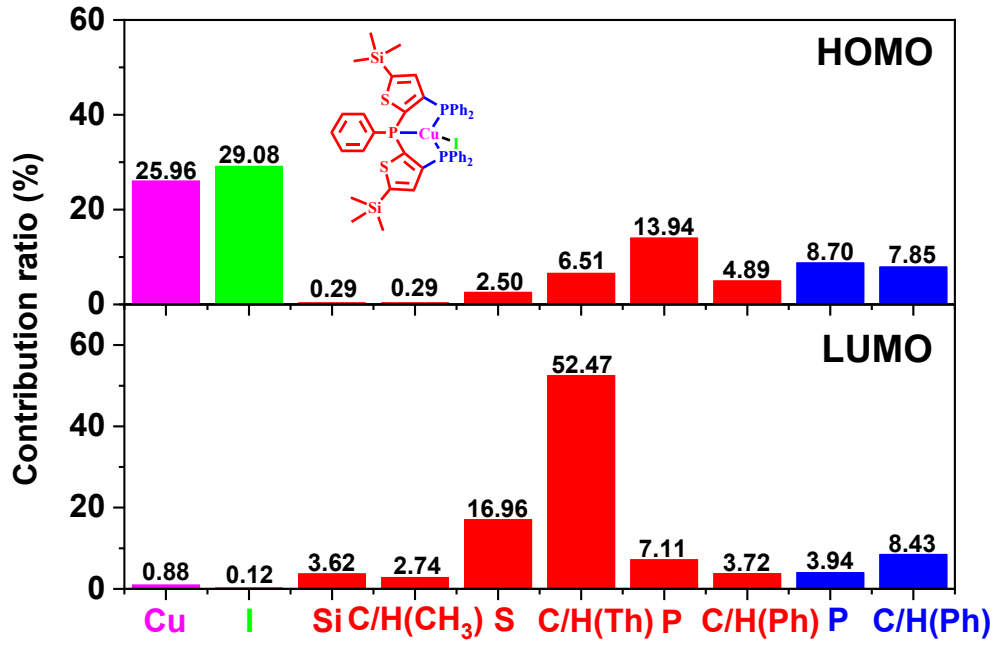

Figure S40. Compositions of the frontier molecular orbitals at optimized S_0 geometry of complex **4**.

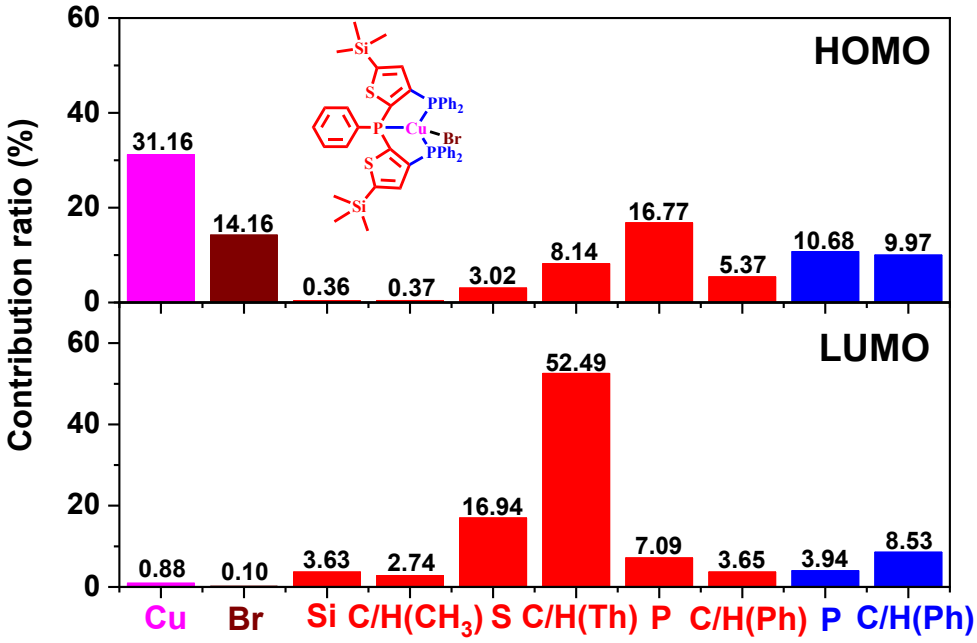

Figure S41. Compositions of the frontier molecular orbitals at optimized S_0 geometry of complex **5**.

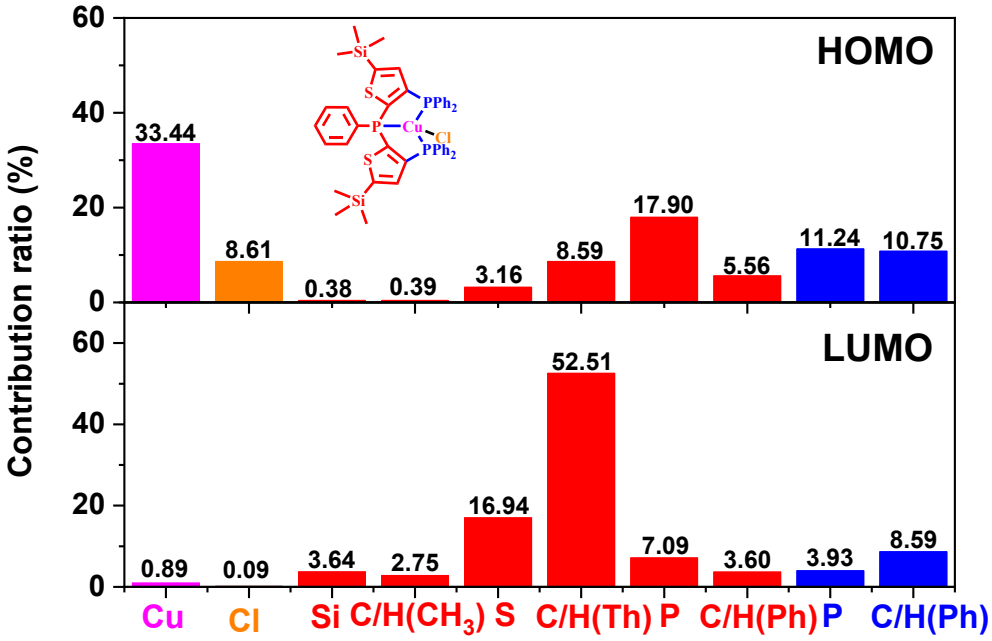

Figure S42. Compositions of the frontier molecular orbitals at optimized S_0 geometry of complex **6**.

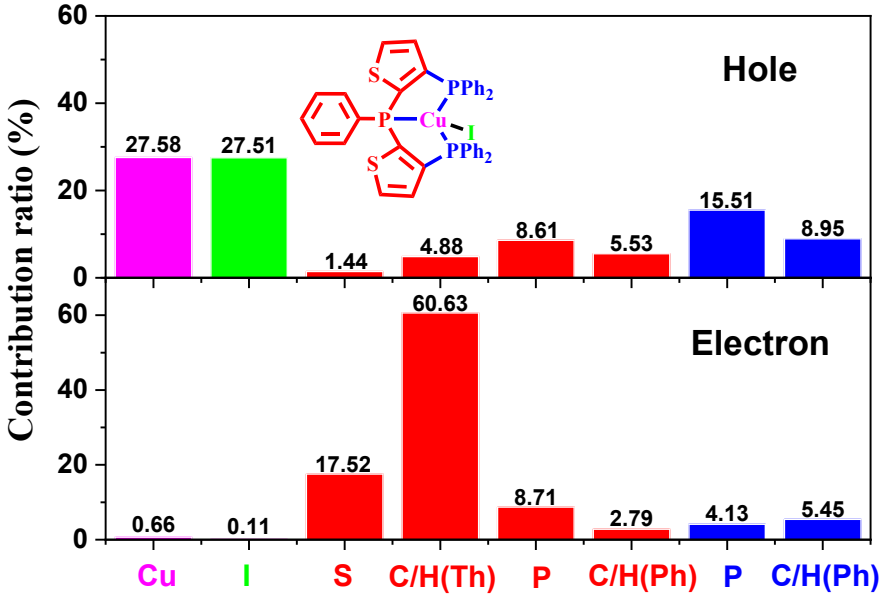

Figure S43. Compositions of the frontier natural transition orbitals at optimized S_1 geometry of complex **1**.

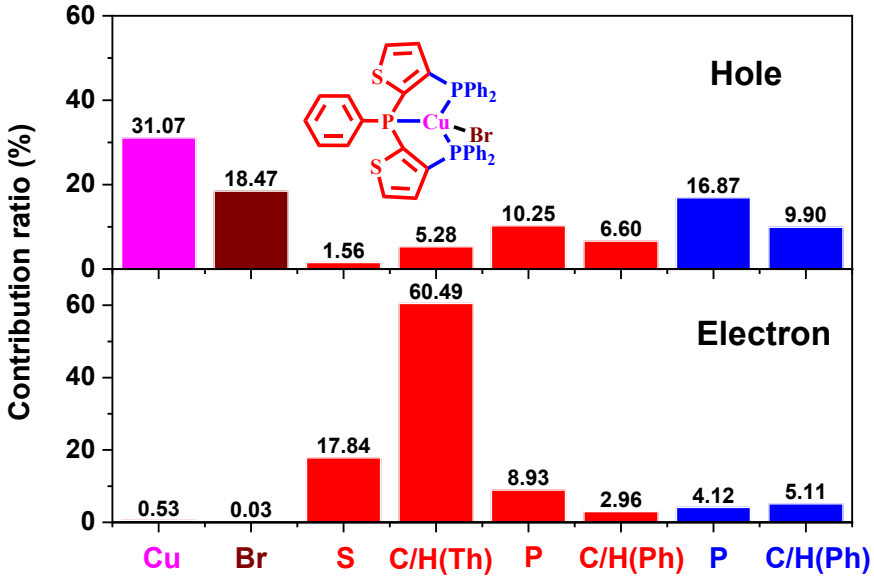

Figure S44. Compositions of the frontier natural transition orbitals at optimized S_1 geometry of complex **2**.

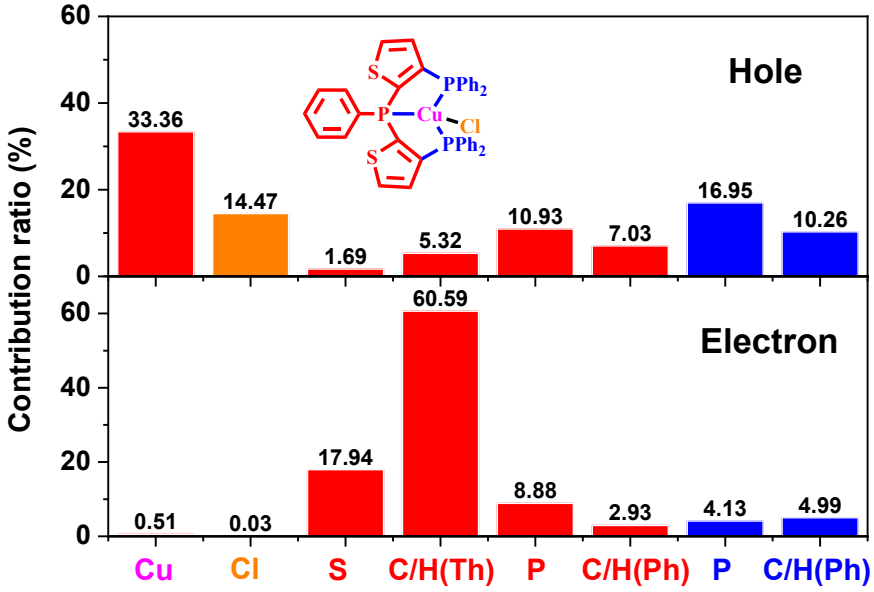

Figure S45. Compositions of the frontier natural transition orbitals at optimized S_1 geometry of complex **3**.

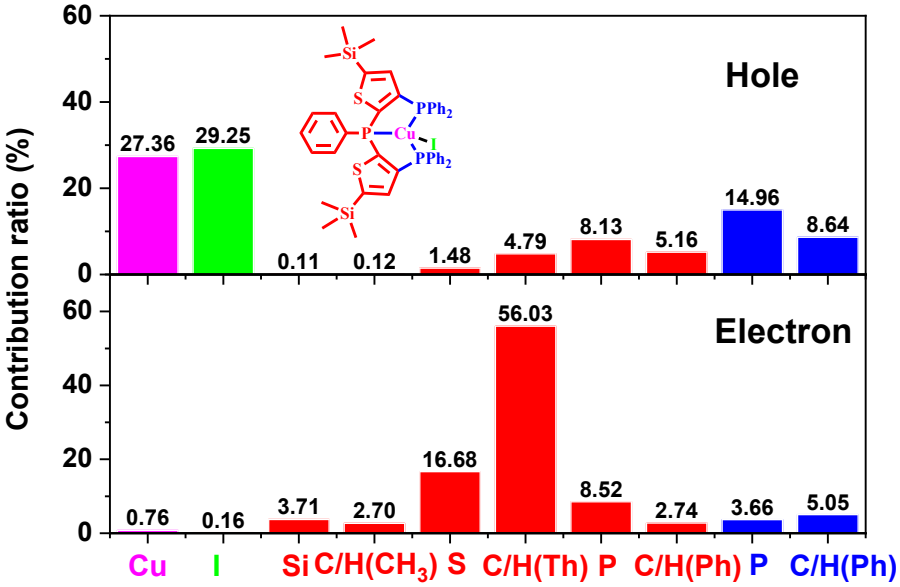

Figure S46. Compositions of the frontier natural transition orbitals at optimized S_1 geometry of complex **4**.

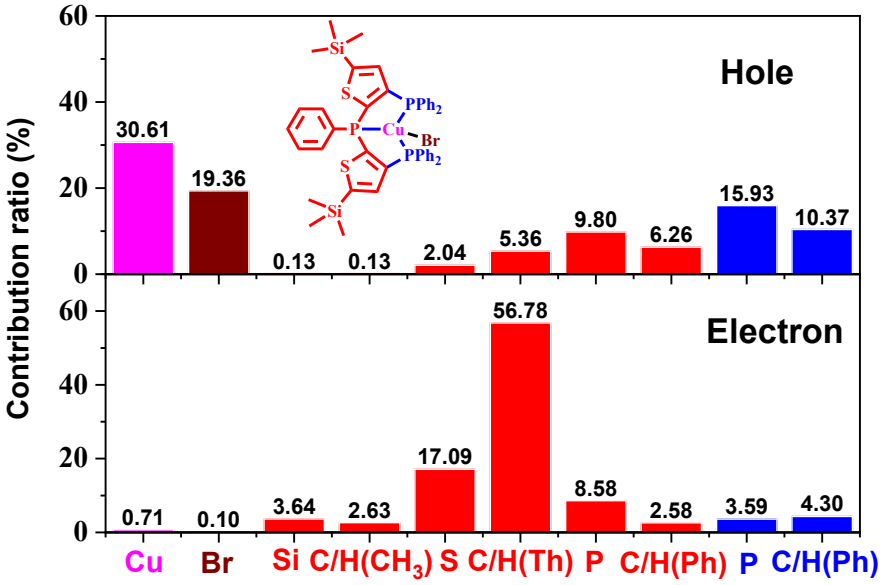

Figure S47. Compositions of the frontier natural transition orbitals at optimized S_1 geometry of complex **5**.

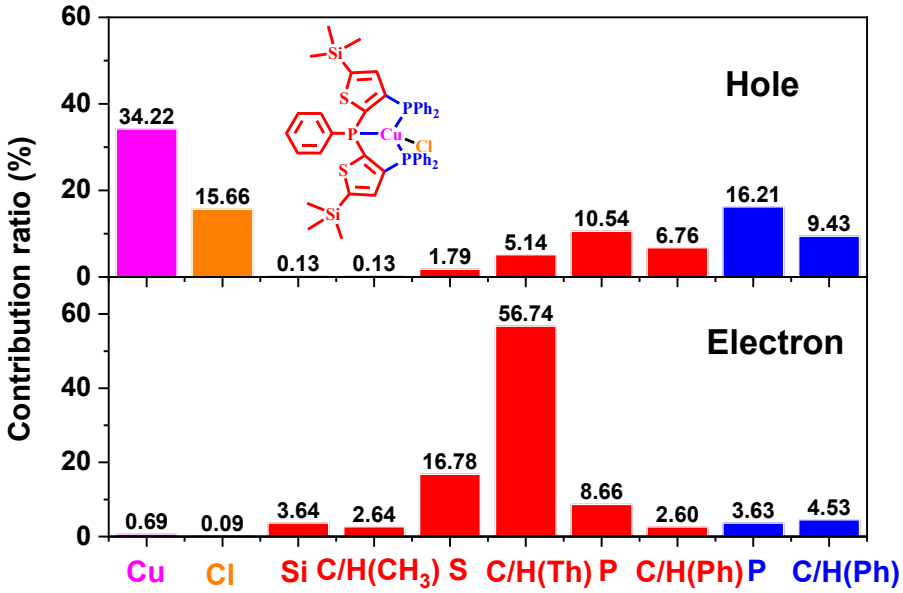

Figure S48. Compositions of the frontier natural transition orbitals at optimized S_1 geometry of complex **6**.

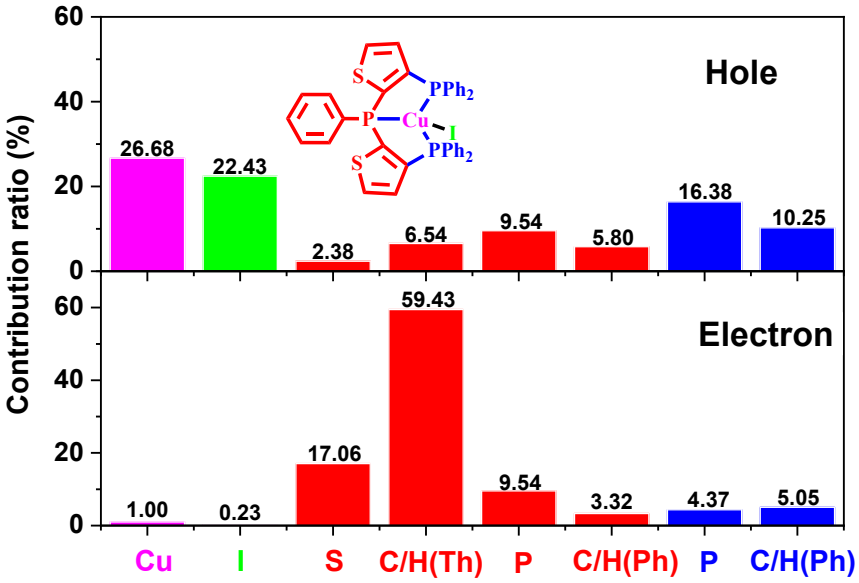

Figure S49. Compositions of the frontier natural transition orbitals at optimized T_1 geometry of complex **1**.

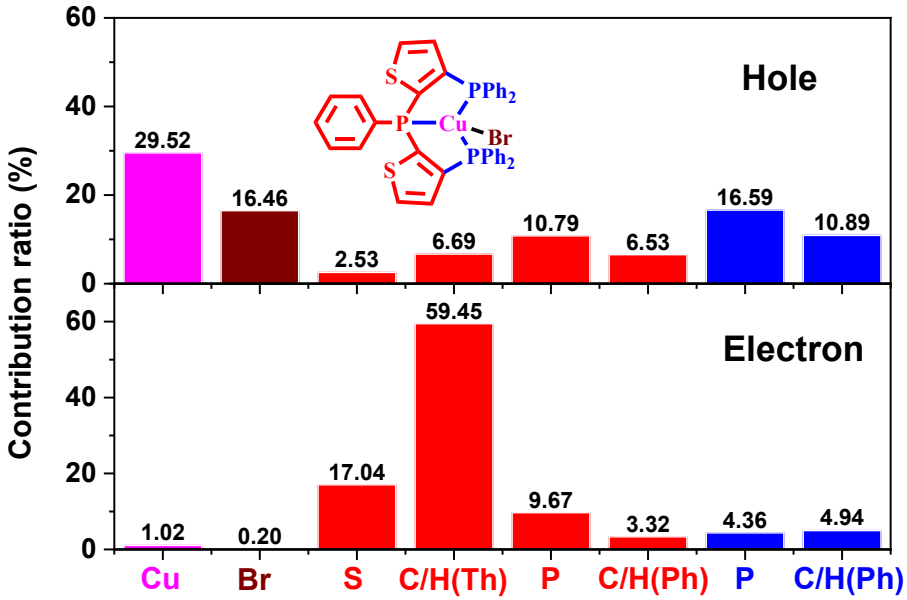

Figure S50. Compositions of the frontier natural transition orbitals at optimized T_1 geometry of complex **2**.

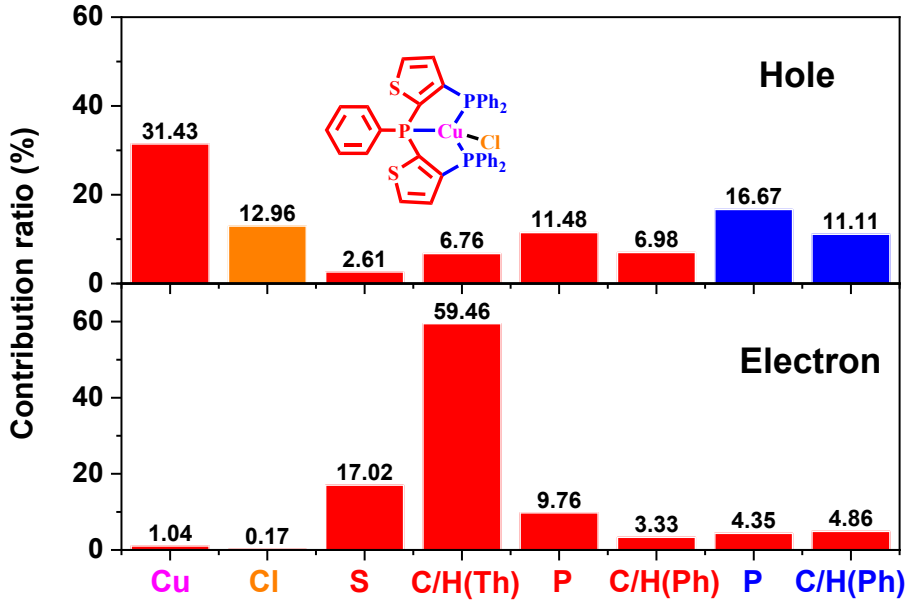

Figure S51. Compositions of the frontier natural transition orbitals at optimized T_1 geometry of complex **3**.

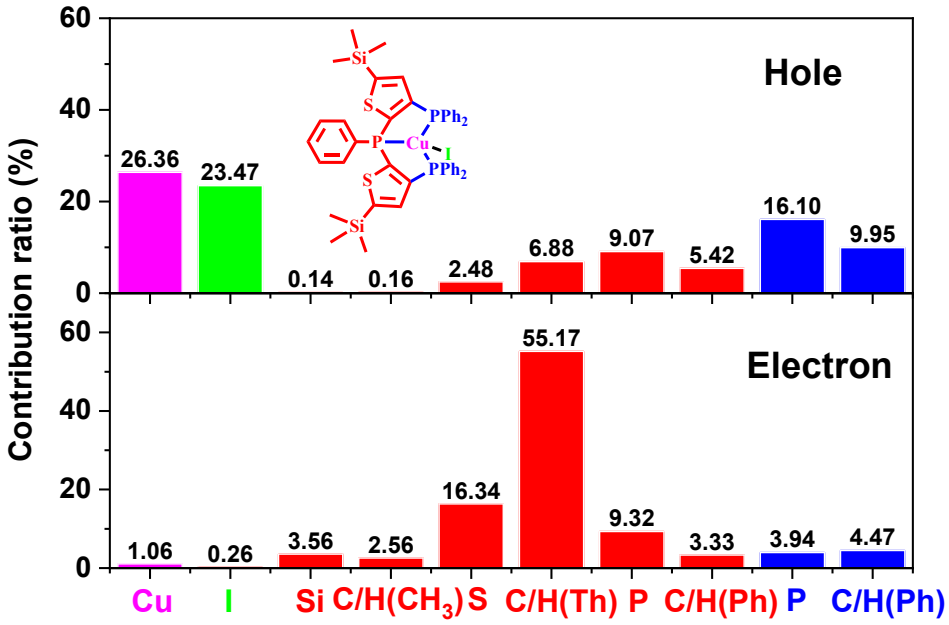

Figure S52. Compositions of the frontier natural transition orbitals at optimized T_1 geometry of complex **4**.

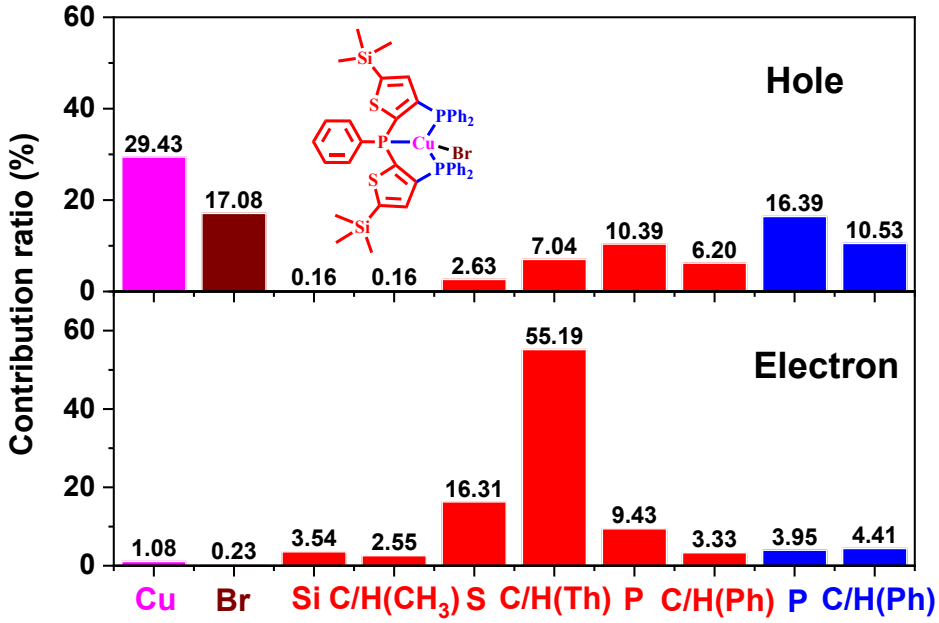

Figure S53. Compositions of the frontier natural transition orbitals at optimized T_1 geometry of complex **5**.

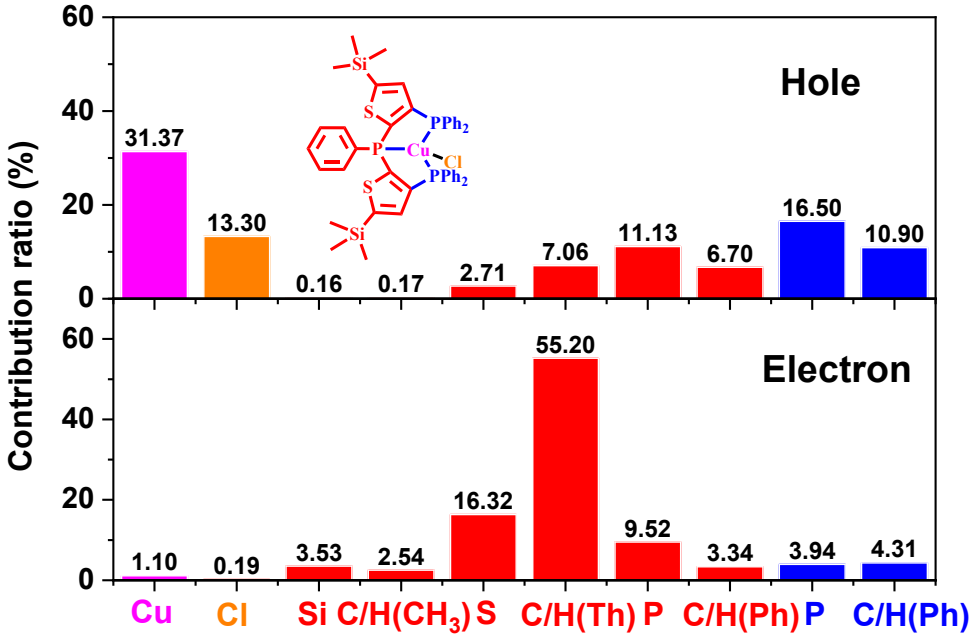

Figure S54. Compositions of the frontier natural transition orbitals at optimized T_1 geometry of complex **6**.

Table S1. Crystallographic data and details for complexes **1–6**.

	1	**2** • CH_2Cl_2	**3**
Empirical formula	$4(C_{38}H_{29}CuIP_3S_2)$	$C_{38}H_{29}CuBrP_3S_2$ • CH_2Cl_2	$C_{38}H_{29}CuClP_3S_2$
Formula weight	3332.32	871.02	741.63
Temperature (K)	100.01(10)	100.00(10)	100.1(5)
Wavelength (Å)	1.54184	1.54184	1.54184
Crystal system	Orthorhombic	Monoclinic	Triclinic
Space group	$Pna2_1$	$P2_1/n$	P–1
a (Å)	78.6606(9)	11.51810(10)	10.5421(2)
b (Å)	11.11090(10)	17.6200(2)	12.8768(2)
c (Å)	17.1137(2)	18.1995(2)	15.4549(2)
α (°)	90	90	97.2800(10)
β (°)	90	97.7150(10)	105.5450(10)
γ (°)	90	90	102.4840(10)
V (Å^3)	14957.2(3)	3660.14(7)	1935.05(6)
Z	4	4	2
ρ (g cm^{-3})	1.480	1.581	1.273
μ (mm^{-1})	9.754	5.995	3.796
F (0 0 0)	6656	1760	760
θ range for data collection (°)	2.816 to 76.665	3.507 to 76.662	3.027 to 76.591
Index ranges	$-99 \leq h \leq 94$ $-13 \leq k \leq 11$ $-21 \leq l \leq 15$	$-13 \leq h \leq 14$ $-19 \leq k \leq 22$ $-22 \leq l \leq 21$	$-12 \leq h \leq 13$ $-16 \leq k \leq 16$ $-17 \leq l \leq 19$
Independent reflections	23860 [R(int) = 0.0773]	7438 [R(int) = 0.0446]	7834 [R(int) = 0.0657]
Completeness to θ = 67.684°	99.1%	99.9%	99.8%
Max. and min. transmission	1.00000 and 0.34829	1.00000 and 0.34896	1.00000 and 0.50231
Gof	1.042	1.048	1.048
Final R indices [I > 2$\sigma(I)$]	R_1 = 0.0648 wR_2 = 0.1629	R_1 = 0.0299 wR_2 = 0.0748	R_1 = 0.0503 wR_2 = 0.1387
R (all data)	R_1 = 0.0727 wR_2 = 0.1694	R_1 = 0.0325 wR_2 = 0.0765	R_1 = 0.0517 wR_2 = 0.1412
Max/min (e Å^3)	1.162 and –1.340	0.780 and –0.820	1.014 and –0.999

	4	**5**	**6**
Empirical formula	$C_{44}H_{45}CuIP_3S_2Si_2$	$C_{44}H_{45}CuBrP_3S_2Si_2$	$C_{44}H_{45}CuClP_3S_2Si_2$
Formula weight	977.45	930.46	886.00
Temperature (K)	100.00(10)	100.01(10)	99.99(10)
Wavelength (Å)	1.54184	1.54184	1.54184
Crystal system	Triclinic	Triclinic	Triclinic
Space group	P−1	P−1	P−1
a (Å)	12.67260(10)	12.61390 (10)	12.57960(10)
b (Å)	13.2191(2)	13.11040(10)	13.03230(10)
c (Å)	14.7902(2)	14.72280(10)	14.72120(2)
α (°)	97.3800(10)	97.2300(10)	96.7840(10)
β (°)	98.9190(10)	99.9810(10)	100.7260(10)
γ (°)	107.4960(10)	107.0170(10)	106.4860(10)
V (Å^3)	2293.82(5)	2252.26(3)	2236.02(3)
Z	2	2	2
ρ (g cm^{-3})	1.415	1.372	1.316
μ (mm^{-1})	8.516	4.331	3.865
F (0 0 0)	992	956	920
θ range for data collection (°)	3.078 to 76.706	3.103 to 76.613	3.107 to 76.693
Index ranges	$-13 \leq h \leq 15$ $-16 \leq k \leq 16$ $-18 \leq l \leq 18$	$-12 \leq h \leq 15$ $-16 \leq k \leq 16$ $-18 \leq l \leq 18$	$-15 \leq h \leq 15$ $-16 \leq k \leq 12$ $-18 \leq l \leq 18$
Independent reflections	9293 [R(int) = 0.0553]	9125 [R(int) = 0.0388]	9036 [R(int) = 0.0464]
Completeness to θ = 67.684°	99.9%	99.9%	99.8%
Max. and min. transmission	1.00000 and 0.51713	1.00000 and 0.39732	1.00000 and 0.62271
Gof	1.062	1.051	1.069
Final R indices [I > 2σ(I)]	R_1 = 0.0346 wR_2 = 0.0917	R_1 = 0.0305 wR_2 = 0.0806	R_1 = 0.0316 wR_2 = 0.0805
R (all data)	R_1 = 0.0360 wR_2 = 0.0929	R_1 = 0.0323 wR_2 = 0.0820	R_1 = 0.0346 wR_2 = 0.0825
Max/min (e Å^3)	1.017 and −1.135	0.497 and −0.612	0.379 and −0.462

Table S2. Computed excitation states for complex **1** in CH_2Cl_2.

State	λ(nm)/*E*(eV)	Configurations	*f*
1	385.9 / 3.21	H→L (97)	0.0185
7	314.3 / 3.94	H-1→L+2 (73); H→L+3 (19)	0.0650
13	298.8 / 4.15	H-1→L+4 (57); H-1→L+5 (3); H→L+5 (31)	0.0690
26	275.7 / 4.50	H-5→L (83); H-1→L+9 (9)	0.1704
34	265.5 / 4.67	H-2→L+4 (87)	0.1092
48	251.9 / 4.92	H-11→L (3); H-9→L (46); H-8→L (9); H-5→L+1 (6); H-3→L+5 (3); H-2→L+7 (17)	0.0503
72	240.1 / 5.16	H-19→L (4); H-16→L (5); H-15→L (14); H-14→L (11); H-13→L (2); H-10→L+1 (2); H-9→L+1 (5); H-8→L+1 (8); H-7→L+1 (9); H-4→L+6 (3); H-3→L+8 (11); H-1→L+13 (4)	0.0863
99	229.8 / 5.39	H-6→L+2 (3); H-5→L+5 (7); H-4→L+9 (26); H-3→L+11 (14); H-1→L+17 (10); H-1→L+18 (7)	0.0837

Table S3. Computed excitation states for complex **2** in CH_2Cl_2.

State	λ(nm)/*E*(eV)	Configurations	*f*
1	383.1 / 3.24	H→L (98)	0.0201
6	311.3 / 3.98	H-2→L (4); H-1→L+2 (56); H→L+3 (33); H→L+4 (3)	0.0835
12	295.3 / 4.20	H-1→L+4 (77); H-1→L+5 (3); H→L+5 (12)	0.0727
17	284.1 / 4.36	H-3→L (92); H-1→L+5 (2)	0.0537
23	273.2 / 4.54	H-5→L (50); H-4→L (5); H-1→L+8 (5); H-1→L+9 (7); H-1→L+10 (4); H→L+10 (22)	0.1135
35	258.0 / 4.81	H-9→L (2); H-4→L+1 (11); H-2→L+4 (37); H-1→L+11 (24); H→L+12 (13)	0.0713
42	251.4 / 4.93	H-11→L (5); H-9→L (56); H-8→L (8); H-5→L+1 (6); H-3→L+2 (6)	0.0650
86	231.3 / 5.36	H-17→L (12); H-14→L+1 (6); H-13→L+1 (17); H-11→L+1 (4); H-9→L+1 (5); H-3→L+7 (10); H-3→L+8 (4); H→L+15 (4); H→L+16 (8)	0.0504
98	227.2 / 5.46	H-20→L (25); H-16→L+1 (4); H-10→L+2 (2); H-6→L+2 (8); H-5→L+5 (4); H-1→L+16 (4); H-1→L+17 (3); H-1→L+18 (3); H→L+17 (2); H→L+18 (3); H→L+19 (3); H→L+21 (8)	0.0665

Table S4. Computed excitation states for complex **3** in CH_2Cl_2.

State	λ(nm)/*E*(eV)	Configurations	*f*
1	383.1 / 3.24	H→L (98)	0.0204
6	310.8 / 3.99	H-1→L+2 (50); H→L+3 (43); H→L+4 (3)	0.0843
12	294.3 / 4.21	H-1→L+4 (81); H-1→L+5 (2); H→L+5 (7); H→L+6 (2)	0.0680
20	276.6 / 4.48	H-3→L (86); H-1→L+7 (6)	0.1500
38	253.0 / 4.90	H-11→L (3); H-10→L (4); H-9→L (13); H-8→L (45); H-7→L (8); H-4→L+1 (9); H-2→L+4 (4)	0.0509
39	251.2 / 4.94	H-11→L (7); H-9→L (39); H-8→L (13); H-5→L+1 (15); H-4→L+1 (7)	0.0684
70	234.1 / 5.30	H-18→L (2); H-16→L (3); H-13→L+1 (2); H-11→L+1 (3); H-10→L+1 (5); H-6→L+2 (4); H-5→L+2 (8); H-4→L+3 (3); H-2→L+9 (3); H-2→L+10 (3); H-1→L+13 (4); H→L+15 (5); H→L+17 (22); H→L+18 (4)	0.0969
94	226.4 / 5.48	H-15→L+1 (30); H-14→L+1 (8); H-8→L+2 (8); H-6→L+3 (2); H-5→L+4 (5); H-3→L+7 (9); H-3→L+8 (6); H-2→L+11 (3)	0.0531

Table S5. Computed excitation states for complex **4** in CH_2Cl_2.

State	λ(nm)/*E*(eV)	Configurations	*f*
1	391.2 / 3.17	H→L (96)	0.0250
7	315.2 / 3.93	H-1→L+2 (77); H→L+3 (15)	0.0656
9	308.5 / 4.02	H-3→L (63); H-1→L+2 (3); H→L+3 (29)	0.0708
20	287.2 / 4.32	H-5→L (52); H-3→L+1 (24); H→L+6 (3); H→L+8 (16)	0.1031
21	286.3 / 4.33	H-5→L (39); H-3→L+1 (24); H-1→L+7 (3); H-1→L+8 (2); H→L+8 (25)	0.1138
34	267.0 / 4.64	H-3→L+2 (7); H-2→L+4 (78); H→L+11 (5)	0.0817
40	260.2 / 4.77	H-7→L (44); H-6→L (5); H-5→L+1 (12); H-4→L+2 (8); H-2→L+6 (15)	0.1174
100	232.5 / 5.33	H-20→L (21); H-18→L (3); H-17→L (4); H-14→L+1 (3); H-13→L+1 (13); H-5→L+5 (4); H-5→L+6 (21); H-3→L+10 (4)	0.0666

Table S6. Computed excitation states for complex **5** in CH_2Cl_2.

State	λ(nm)/*E*(eV)	Configurations	*f*
1	388.1 / 3.19	H→L (98)	0.0273
6	314.5 / 3.94	H-2→L (87); H-1→L+2 (7); H→L+3 (2)	0.0688
7	311.9 / 3.98	H-2→L (10); H-1→L+2 (59); H→L+3 (26); H→L+4 (2)	0.0699
12	296.7 / 4.18	H-1→L+4 (51); H-1→L+5 (5); H→L+5 (35)	0.0759
14	290.9 / 4.26	H-3→L (59); H-2→L+1 (5); H-1→L+5 (3); H→L+6 (26)	0.1108
20	281.4 / 4.41	H-4→L (87); H-1→L+6 (2); H-1→L+7 (3)	0.0689
38	258.0 / 4.81	H-9→L (15); H-8→L (28); H-5→L+1 (17); H-4→L+1 (8); H-2→L+4 (13); H-2→L+6 (2); H→L+12 (3)	0.1740
52	247.4 / 5.01	H-12→L (15); H-11→L (5); H-6→L+1 (12); H-2→L+6 (3); H-2→L+7 (26); H→L+12 (12); H→L+13 (10); H→L+16 (2)	0.0640
59	243.4 / 5.09	H-16→L (32); H-15→L (2); H-13→L (2); H-7→L+1 (3); H-5→L+2 (13); H-3→L+4 (6); H-2→L+9 (3); H→L+12 (2); H→L+14 (2); H→L+15 (4); H→L+16 (9)	0.0609

Table S7. Computed excitation states for complex **6** in CH_2Cl_2.

State	λ(nm)/*E*(eV)	Configurations	*f*
1	388.1 / 3.19	H→L (98)	0.0280
6	312.3 / 3.97	H-2→L (11); H-1→L+2 (55); H→L+3 (28)	0.0907
7	309.6 / 4.00	H-2→L (85); H-1→L+2 (6); H→L+3 (6)	0.0655
12	295.9 / 4.19	H-1→L+4 (58); H-1→L+5 (5); H→L+5 (28); H→L+7 (2)	0.0824
15	287.6 / 4.31	H-3→L (50); H-2→L+1 (24); H-1→L+5 (13); H→L+7 (4); H→L+8 (5)	0.0610
17	286.3 / 4.33	H-3→L (42); H-2→L+1 (25); H-1→L+5 (20); H→L+6 (3); H→L+8 (4)	0.1653
34	258.9 / 4.79	H-9→L (11); H-8→L (19); H-7→L (40); H-5→L+1 (2); H-3→L+1 (4); H-2→L+3 (6); H-2→L+4 (5)	0.0976
37	256.7 / 4.83	H-9→L (11); H-8→L (7); H-7→L (3); H-4→L+1 (5); H-2→L+4 (62); H-1→L+11 (2)	0.0660
73	235.7 / 5.26	H-17→L (3); H-13→L+1 (2); H-10→L+2 (2); H-5→L+2 (3); H-4→L+3 (13); H-3→L+5 (3); H-2→L+9 (2); H-1→L+14 (5); H-1→L+15 (5); H-1→L+16 (8); H→L+16 (3); H→L+17 (15); H→L+20 (4)	0.0693
91	229.6 / 5.40	H-16→L+1 (6); H-15→L+1 (4); H-13→L+1 (5); H-11→L+1 (13); H-10→L+1 (10); H-7→L+2 (2); H-6→L+2 (5); H-5→L+3 (2); H-5→L+4 (3); H-3→L+8 (7); H→L+20 (4); H→L+21 (3); H→L+22 (3)	0.0715

Table S8. Electrochemical data, energy levels, energy gaps of the complexes **1**–**6**.

Complex	E_{ox1} (V)[a]	$E_{on\text{-}s}$[b]	ΔE_g (eV)[c]	E_{HOMO} (eV)[d]	E_{LUMO} (eV)[e]
1	0.65	0.12	2.97	–4.86	–1.92
2	0.78	0.20	2.99	–4.94	–1.95
3	0.75	0.21	2.99	–4.95	–1.96
4	0.62	0.10	2.90	–4.84	–1.94
5	0.72	0.16	2.92	–4.90	–1.98
6	0.71	0.18	2.92	–4.92	–2.00

[a] Experimental peak potentials of oxidation (*vs*. SCE).

[b] The onset potentials of oxidation (*vs.* Fc/Fc^+).

[c] Estimated from the onset wavelengths of the absorption spectra measured in CH_2Cl_2.

[d] $E_{HOMO} = -4.74 - E_{on\text{-}s.}$

[e] $E_{LUMO} = E_{HOMO} + \Delta E_{g.}$

6. References

(1) J. Y. Fang, C. Chen, G. Chen, Y. L. Liu, Z. Chen and L. Liu. *J. Hubei Univ. (Natural Science)*, 2024, **46**, 356–362.

(2) *SAINT Reference Manual*, Siemens Energy and Automation, Madison, WI, 1994.

(3) G. M. Sheldrick, *SADABS*, *Empirical Absorption Correction Program*, University of Göttingen, Göttingen, Germany, 1997.

(4) G. M. Sheldrick, *SHELXTL Reference Manual*, *Version 5.1*, Siemens Energy and Automation, Madison, WI, 1997.

(5) M. J. Frisch, G. W. Trucks, H. B. Schlegel, G. E. Scuseria, M. A. Robb, J. R. Cheeseman, G. Scalmani, V. Barone, G. A. Petersson, H. Nakatsuji, X. Li, M. Caricato, A. V. Marenich, J. Bloino, B. G. Janesko, R. Gomperts, B. Mennucci, H. P. Hratchian, J. V. Ortiz, A. F. Izmaylov, J. L. Sonnenberg, D. Williams-Young, F. Ding, F. Lipparini, F. Egidi, J. Goings, B. Peng, A. Petrone, T. Henderson, D. Ranasinghe, V. G. Zakrzewski, J. Gao, N. Rega, G. Zheng, W. Liang, M. Hada, M. Ehara, K. Toyota, R. Fukuda, J. Hasegawa, M. Ishida, T. Nakajima, Y. Honda, O. Kitao, H. Nakai, T. Vreven, K. Throssell, J. A. Montgomery, Jr., J. E. Peralta, F. Ogliaro, M. J. Bearpark, J. J. Heyd, E. N. Brothers, K. N. Kudin, V. N. Staroverov, T. A. Keith, R. Kobayashi, J. Normand, K. Raghavachari, A. P. Rendell, J. C. Burant, S. S. Iyengar, J. Tomasi, M. Cossi, J. M. Millam, M. Klene, C. Adamo, R. Cammi, J. W. Ochterski, R. L. Martin, K. Morokuma, O. Farkas, J. B. Foresman, and D. J. Fox, *Gaussian 16*, *Revision A.03*, Gaussian Inc., Wallingford CT, 2016.

(6) T. Lu, F.W. Chen, *Acta Chim. Sinica*, 2011, **69**(20), 2393–2406.

(7) T. Lu, F.W. Chen, *J. Comput. Chem.* 2012, **33**(5), 580–592.